Engineering Fracture Mechanics 77 (2010) 415–436

Contents lists available at ScienceDirect

Engineering Fracture Mechanics

journal homepage: www.elsevier.com/locate/engfracmech

# *J* and CTOD estimation procedure for circumferential surface cracks in pipes under bending

Mario S.G. Chiodo, Claudio Ruggieri *

*Department of Naval Architecture and Ocean Engineering, Av. Prof. Mello Moraes, 2231 (PNV-EPUSP), São Paulo – SP 05508-030, Brazil*

ARTICLE INFO

*Article history:*
Received 21 April 2009
Received in revised form 1 September 2009
Accepted 8 October 2009
Available online 21 October 2009

*Keywords:*
*J*-integral
CTOD
Fully plastic solutions
EPRI methodology
Circumferential surface crack
Pipeline
Defect assessments

ABSTRACT

This work provides an estimation procedure to determine the *J*-integral and CTOD for pipes with circumferential surface cracks subjected to bending load for a wide range of crack geometries and material (hardening) based upon fully-plastic solutions. A summary of the methodology upon which *J* and CTOD are derived sets the necessary framework to determine nondimensional functions $h_1$ and $h_2$ applicable to a wide range of crack geometries and material properties characteristic of structural, pressure vessel and pipeline steels. The extensive nonlinear, 3-D numerical analyses provide a definite full set of solutions for *J* and CTOD which enters directly into fitness-for-service (FFS) analyses and defect assessment procedures of cracked pipes and cylinders subjected to bending load.



## 1. Introduction

Fracture assessments of circumferential surface flaws in structural components play an important role in current applications of fitness-for-service (FFS) procedures for repair decisions and life-extension programs of critical engineering structures. These crack-like defects are most often formed during in-service operation and exposure to aggressive environment (such as, for example, stress corrosion assisted cracks) or during welding fabrication. Structural components falling into this category include girth welds made in field conditions for deep water steel catenary risers. More efficient and faster installation methods for these structures now underway employ the pipe reeling process which allows welding and inspection to be conducted at onshore facilities (see e.g. [1,2]). The welded pipe is coiled around a large diameter reel on a vessel and then unreeled, straightened and finally deployed to the sea floor. However, the reeling process subjects the pipe to high levels of bending load and plastic deformation with potential strong impact on unstable crack propagation of undetected (circumferential) flaws at girth welds. With the increasing demand to meet more stringent requirements of structural safety while, at the same time, complying with current economical constraints, the specification of acceptable flaw sizes and safety margins remains essential.

Defect assessment procedures of cracked pipes and cylinders under varying loading conditions rely heavily on the accurate evaluation of crack driving forces, such as the (Mode I) linear elastic stress intensity factor, $K_I$, and the elastic–plastic *J*-integral (or, equivalently, the crack tip opening displacement, CTOD or $\delta$) [3–6]. These measures of crack-tip loading provide a means to correlate the severity of crack-like defects to the operating conditions in terms of the simple axiom that fracture occurs when the applied crack driving force reaches a critical value as given by $K_{Ic}$, $J_c$ or $\delta_c$. Previous research efforts have

* Corresponding author. Tel.: +55 11 30915350; fax: +55 11 30915717.
*E-mail address:* claudio.ruggieri@usp.br (C. Ruggieri).

0013-7944/$ - see front matter © 2009 Elsevier Ltd. All rights reserved.
doi:10.1016/j.engfracmech.2009.10.001

**Nomenclature**

| | |
|---|---|
| $a$ | crack depth |
| $b$ | remaining crack ligament |
| $c$ | circumferential crack half-length |
| $d_n$ | dimensionless constant which relates $J$ and CTOD |
| $g_{ij}$ | dimensionless function of spatial position and strain hardening |
| $h_1$ | dimensionless proportionality parameter between $J_p$ and applied loading |
| $h_2$ | dimensionless proportionality parameter between $\delta_p$ and applied loading |
| $m$ | dimensionless constant which relates $J$ and CTOD under small scale yielding (SSY) |
| $n$ | Ramberg–Osgood strain hardening exponent |
| $n_j$ | outward normal (unit vector) to $\Gamma$ |
| $r$ | distance to the crack tip (polar or cylindrical radial coordinate) |
| $t$ | wall thickness |
| $u_i$ | cartesian components of displacement |
| $\overline{B}$ | strain–displacement matrix based on the $\overline{\boldsymbol{B}}$-bar formulation |
| CTOD | crack tip opening displacement |
| $D_e$ | external pipe diameter |
| $E, E'$ | Young's modulus under plane stress (plane strain) conditions |
| EPRI | Electric Power Research Institute |
| FFS | fitness-for-service |
| $G_5$ | influence coefficient to compute the stress intensity factor |
| $I_n$ | integration constant for the HRR fields |
| $J$ | $J$-Integral |
| $J_2$ | second invariant of the stress deviator tensor |
| $J_c$ | critical value of $J$ Integral |
| $J_e$ | elastic component of the $J$ -Integral |
| $J_p$ | plastic component of the $J$ -Integral |
| $\bar{J}_p$ | normalized plastic component of $J$-integral |
| $J_{pred}$ | predicted value of $J$ -integral |
| $J_{reel}$ | maximum $J$ -value attained in the reeling simulation |
| $J_t$ | $J$-value corresponding to the limit bending moment using the material's ultimate tensile stress |
| $J_y$ | $J$-value corresponding to the limit bending moment using the material's yield stress |
| $K_I$ | stress intensity factor |
| $K_{Ic}$ | critical value of the stress intensity factor |
| LLD | load line displacement |
| $\ell$ | characteristic length for the cracked component |
| $M$ | applied bending moment |
| $M_0$ | limit bending moment |
| $P$ | generalized applied load |
| $P_0$ | generalized limit load |
| $Q_s$ | flaw shape parameter |
| $R_b$ | bending radius |
| $R_e$ | external radius of pipe |
| $R_i$ | internal radius of pipe |
| $R_m$ | mean radius of pipe |
| $W$ | structural component width |
| $W_s$ | stress-work density |
| $\alpha$ | dimensionless parameter of the Ramberg–Osgood model |
| $\beta$ | angular parameter related to the circumferential surface crack geometry |
| $\Gamma$ | arbitrary counter-clockwise path around the crack tip |
| $\delta$ | crack tip opening displacement |
| $\delta_c$ | critical value of the crack tip opening displacement |
| $\delta_e$ | elastic component of crack tip opening displacement |
| $\delta_p$ | plastic component of crack tip opening displacement |
| $\bar{\delta}_p$ | normalized plastic component of crack tip opening displacement |
| $\delta_t$ | $\delta$-value corresponding to the limit bending moment using the material's ultimate tensile stress |
| $\delta_y$ | $\delta$-value corresponding to the limit bending moment using the material's yield stress |
| $\Delta$ | load line displacement |
| $\bar{\varepsilon}$ | true (logarithmic) strain |
| $\varepsilon_e$ | elastic strain component |

| | |
|---|---|
| $\varepsilon_p$ | plastic strain component |
| $\varepsilon_{ys}$ | yield strain |
| $\varepsilon_z^b$ | longitudinal bending strain |
| $\varepsilon_{z,max}^b$ | maximum value of longitudinal bending strain |
| $\zeta_k$ | coefficients for the polynomial fitting of factor $h_2$ |
| $\eta$ | nondimensional parameter describing the plastic contribution to the strain energy |
| $\theta$ | half angle describing the surface crack length |
| $\nu$ | Poisson's ratio |
| $\xi_k$ | coefficients for the polynomial fitting of factor $h_1$ |
| $\rho_0$ | initial crack tip blunting radius |
| $\bar{\sigma}$ | true stress |
| $\sigma_b$ | global or net-section bending stress |
| $\sigma_{ij}$ | cartesian components of stress |
| $\tilde{\sigma}_{ij}$ | dimensionless function of HRR singularity |
| $\sigma_{uts}$ | ultimate tensile stress |
| $\sigma_{ys}$ | yield stress |

provided an extensive body of $K_I$ solutions for a variety of crack configurations, including circumferentially cracked cylinders, which are readily available through several compendia [7–11]. In contrast, a full set of $J$ and CTOD solutions for varying crack geometries and loading modes directly connected to the description of fracture behavior under large scale yielding conditions is still lacking.

Current evaluation procedures for $J$ focus primarily on developing estimation schemes for its plastic component, denoted $J_p$. These methodologies have evolved essentially along three lines of development: (1) estimation procedures relating the plastic contribution to the strain energy and $J$; (2) fully plastic descriptions of $J$ based upon HRR-controlled crack-tip fields and limit load solutions and (3) approximate descriptions of $J$ derived from the concept of a reference stress coupled with stress intensity factor solutions. The first approach employs a plastic $\eta$-factor introduced by Sumpter and Turner [12] to relate the macroscale crack driving force ($J$ and CTOD) to the area under the load vs. load line displacement (or crack mouth opening displacement) for cracked configurations (see also Refs. [13,14]). Because of its relative ease with which the load–displacement records can be measured in conventional test specimens, the method is most suited for testing protocols to measure fracture toughness such as ASTM E1820 [15]. The second approach derives from previous work of Kumar et al. [16] building upon early investigation of Shih and Hutchinson [17] to introduce an estimation procedure for $J_p$ applicable to elastic–plastic materials following a power hardening law such as the Ramberg–Osgood model [5,10,18]. Here, $J_p$ is expressed in the general form $J_p \propto h_1(a/W, \ell, n)(P/P_0)^{n+1}$ where $a$ is the crack size, $W$ denotes the component width, $\ell$ represents a characteristic length for the cracked component, $n$ is the Ramberg–Osgood strain hardening exponent, $P$ defines a generalized load and $P_0$ is the corresponding (plastic) limit load. Factor $h_1$ represents a nondimensional parameter dependent upon crack size, component geometry and strain hardening properties which simply scales $J_p$ with $(P/P_0)^{n+1}$. The method became widely known as the EPRI methodology and has later been expanded by Zahoor [19] to include additional geometries such as circumferentially and axially cracked pipes under tensile and bending loads. However, these $J$ solutions for circumferentially cracked pipes subjected to bending remain limited to very few crack geometries and strain hardening properties. The third approach, most often referred to as the reference stress approach, is essentially a modification of the EPRI methodology proposed by Ainsworth [20] to reflect more closely the flow behavior of real materials, particularly high hardening materials such as austenitic stainless steels. Moreover, this approach enables evaluation of $J_p$ from simply using available stress intensity factor solutions for the cracked component in connection with the adoption of parameter $h_1$ defined for a linear material in which $n = 1$.

While all these procedures share much in common, each method has certain relative advantages and disadvantages in fracture mechanics applications. In particular, both the fully plastic (EPRI) and the reference stress methods prove sufficiently applicable for a broad range of crack geometries and loading modes. Further, they provide essentially similar estimates of crack driving forces for low to moderate deformation levels, as measured by $J$ (CTOD), when the material's stress–strain behavior is adequately described by a power hardening law such as the Ramberg–Osgood model. However, this picture becomes potentially more complex as the evolving plasticity progresses from contained to fully yielded conditions, particularly for moderate to low hardening materials. Because parameter $h_1$ depends rather strongly on the strain hardening exponent (this issue is addressed later in Section 4), adopting $h_1$ for a linear material with $n = 1$ in Ainsworth's model can lead to unacceptably large errors in $J$ estimations, especially for moderate to large $n$-values. While previous exploratory analyses by Anderson [5] have shown that both approaches provide similar predictions of critical crack sizes in center cracked panels, extension of these methodologies in accurate descriptions of crack-tip driving forces (as measured by $J$ and CTOD) for circumferentially cracked pipes under conditions of varying cracking geometries, material properties and loading modes remains untested. These observations clearly underlie the need of reliable and yet simple evaluation procedures for crack-tip driving forces in advanced defect assessment methodologies applicable to elastic–plastic and fully plastic conditions.

The extension of fully plastic solutions for $J$ and CTOD crack-tip driving forces for pipes with circumferential surface cracks subjected to bending load for a wide range of crack geometries and strain hardening properties is the focus of this paper. The present investigation broadens the applicability of current evaluation procedures for $J$ and CTOD which enter directly into structural integrity analyses and flaw tolerance criteria. The presentation begins with a summary of the fully-plastic solution upon which $J$ and CTOD are derived which forms the basis of the adopted framework to determine the elastic–plastic crack-tip driving forces for the analyzed cracked configurations. This is followed by the description of extensive 3-D nonlinear analyses of circumferentially cracked pipes with surface flaws having different crack depth ($a$) over pipe wall thickness ($t$) ratios and varying crack length for different strain hardening properties. The 3-D results cover a large set of dimensionless functions relating the elastic–plastic crack-tip driving forces with the applied (remote) bending moment. As a further refinement, a sensitivity analysis to assess the robustness of the $R$–$O$ power-law fit in characterizing the crack-tip driving forces is conducted. The study also examines an exploratory comparison between the resulting fully-plastic solutions and finite element analyses of circumferentially cracked pipes subjected to reeling. The investigation provides a fairly comprehensive body of numerical solutions for $J$ and CTOD in circumferentially cracked pipes subjected to bending while, at the same time, gaining additional understanding of the potential applicability of fully plastic solutions in cracked structural components.

## 2. Fully plastic solutions for $J$ and CTOD

Advanced procedures for defect assessment of engineering components and structures made of materials with sufficient toughness require the knowledge of elastic–plastic crack-tip driving forces as characterized by the $J$-integral and CTOD. While detailed, nonlinear finite element analyses now available imposes essentially no restrictions on direct evaluation of these fracture parameters for a large variety of crack configurations, material properties and loading conditions, the much higher level of required effort, particularly in 3-D applications, still underlies the need of simplified $J$ and CTOD estimation techniques in routine defect assessments. A relatively straightforward procedure to evaluate $J$ and CTOD in the elastic–plastic and fully plastic regimes based upon the EPRI methodology [15,18] proves a viable and yet simple analytical tool in conventional fracture analyses.

This section introduces the essential features of the theoretical framework needed to determine $J$ and CTOD for circumferentially cracked cylinders and pipes based upon fully plastic solutions for power hardening materials. The description that follows draws heavily on the early work of Shih and Hutchinson [17], Kumar et al. [16], Anderson [5] and Kanninen and Popelar [21] while, at the same time, providing the basis to develop a fully plastic analysis for a cracked body in which the material is conveniently characterized by a power hardening stress–strain behavior. Attention is directed to estimation solutions applicable to stationary cracks subjected to monotonically increasing loading (deformation). Subsequent development focuses on a simpler extension of the $J$ and CTOD evaluation procedure to circumferentially cracked cylinders and pipes under bending load.

### 2.1. $J$ and CTOD estimation procedure for power hardening materials

Development of fully plastic solutions for $J$ and CTOD begins by considering an elastic–plastic power-hardening model to describe the material's stress–strain behavior in the form

$$\frac{\bar{\varepsilon}}{\varepsilon_{ys}} = \frac{\bar{\sigma}}{\sigma_{ys}} + \alpha\left(\frac{\bar{\sigma}}{\sigma_{ys}}\right)^{n} \tag{1}$$

where $\bar{\sigma}$ is the true stress, $\bar{\varepsilon}$ is the true (logarithmic) strain, $\sigma_{ys}$ defines the yield stress, most often assigned the value of the 0.2% proof stress, $\varepsilon_{ys} = \sigma_{ys}/E$ is the corresponding reference strain with $E$ representing the (longitudinal) elastic modulus, $\alpha$ is a dimensionless constant and $n$ defines the strain hardening exponent. The previous Eq. (1) is also known as the Ramberg–Osgood model [5,10,18] and is widely adopted for fitting uniaxial stress–strain tensile data.

Upon consideration of a fully plastic cracked body in which the elastic strains, $\varepsilon_e$, are assumed to remain vanishingly small compared to the plastic strains, $\varepsilon_p$, the stress–strain behavior defined by Eq. (1) reduces to a pure power law where $\varepsilon_p \propto \alpha(\bar{\sigma}/\sigma_{ys})^n$. Under such conditions and within distances sufficiently close to the crack tip, the general form of the asymptotic crack-tip stress fields well inside the plastic region is given by the HRR singularity in the form [5,6,21]

$$\sigma_{ij} = \sigma_{ys}\left(\frac{J}{\alpha\varepsilon_{ys}\sigma_{ys}I_n r}\right)^{1/(n+1)} \tilde{\sigma}_{ij}(n,\varphi) \tag{2}$$

where $(r,\varphi)$ are cylindrical coordinates centered at the crack tip. Here, $I_n$ is an integration constant that depends on $n$ and $\tilde{\sigma}_{ij}(r,\varphi)$ is a dimensionless function of $n$ and $\varphi$. For the purpose of subsequent development, the above equation is conveniently solved for $J$ in the form

$$J = \frac{\alpha\varepsilon_{ys}\sigma_{ys}I_n r}{[\tilde{\sigma}_{ij}(n,\varphi)]^{(n+1)}}\left(\frac{\sigma_{ij}}{\sigma_{ys}}\right)^{(n+1)} \tag{3}$$

We now consider Ilyushin's theorem [6,21,22] which states that the fully plastic stresses simply scale with the (generalized) applied load, $P$, such as $\sigma_{ij} = g_{ij}(r,\varphi,n)P$ where the quantity $g_{ij}$ is a dimensionless function of spatial position and strain hardening but it is independent of applied load. Noting that $J \propto (\sigma_{ij})^{n+1}$ in the previous HRR solution, it follows that $J$ scales with $P^{n+1}$. Consequently, the fully plastic $J$ given by Eq. (3) can be expressed as

$$J = \alpha\varepsilon_{ys}\sigma_{ys}bh_1(a/W,\ell,n)\left(\frac{P}{P_0}\right)^{n+1} \tag{4}$$

where $a$ is the crack size, $W$ denotes the cracked component width, $b = W - a$ defines the uncracked ligament, $\ell$ represents a characteristic length for the cracked component and $P_0$ is the (generalized) limit load. In the above expression, $h_1$ is a dimensionless factor dependent upon crack size, component geometry and strain hardening properties.

The previous solution for $J$ is essentially applicable for fully plastic cracked configurations in which the elastic strains are vanishingly small, particularly within the annular region surrounding the crack tip where Eq. (3) and the condition $J \propto P^{n+1}$ hold true. A convenient approach to extend the $J$-evaluation procedure over the full range of elastic–plastic loading follows from earlier work of Shih and Hutchinson [17] to yield an additive decomposition of $J$ into elastic, $J_e$, and plastic, $J_p$, components given by

$$J = J_e(a, n = 1) + J_p(a,n) \tag{5}$$

The first term on the right side of Eq. (5) implies that $J_e \propto P^2$ which enables defining $J_e$ by the energy release rate for a linear elastic cracked body under Mode I deformation in the standard form

$$J_e = \frac{K_I^2}{E'} \tag{6}$$

where $K_I$ denotes the (Mode I) elastic stress intensity factor for the cracked configuration and $E' = E/(1-\nu^2)$ with $\nu$ representing the Poisson's ratio. To maintain consistency with the above procedure, the plastic component of the $J$-integral is directly derived from the use of Eq. (4) but with $J$ replaced by $J_p$.

The previous framework also applies when the CTOD is adopted to characterize the crack-tip driving force. Following the earlier analysis for the $J$-integral and using the connection between $J$ and the crack-tip opening displacement ($\delta$) [4,5] given by

$$\delta = \frac{d_n J}{\sigma_{ys}} \tag{7}$$

in which $d_n$ is a dimensionless constant, a formally similar expression to Eq. (5) is employed to yield

$$\delta = \delta_e + \delta_p \tag{8}$$

where the elastic component, $\delta_e$, is given by

$$\delta_e = \frac{K_I^2}{m\sigma_{ys}E'} \tag{9}$$

in which $m$ is a dimensionless constant and the plastic component, $\delta_p$, is expressed as

$$\delta_p = \alpha\varepsilon_{ys}bh_2(a/W,\ell,n)\left(\frac{P}{P_0}\right)^{n+1} \tag{10}$$

with $h_2$ defining a dimensionless factor dependent upon crack size, component geometry and strain hardening properties. It follows from the previous relationship between $J$ and CTOD given by Eq. (7) that $h_2 = d_n h_1$.

### 2.2. Extension to circumferentially cracked pipes

To introduce an estimation procedure of $J$ and CTOD for a cylinder or pipe having a circumferential surface crack based upon the previous fully-plastic solutions, consider the crack configuration subjected to bend loading illustrated in Fig. 1. The above methodology can be extended in straightforward manner to define $J_p$ and $\delta_p$ for this crack geometry by the following expressions

$$J_p = \alpha\varepsilon_{ys}\sigma_{ys}bh_1(a/t, D_e/t, \theta, n)\left(\frac{M}{M_0}\right)^{n+1} \tag{11}$$

and

$$\delta_p = \alpha\varepsilon_{ys}bh_2(a/t, D_e/t, \theta, n)\left(\frac{M}{M_0}\right)^{n+1} \tag{12}$$

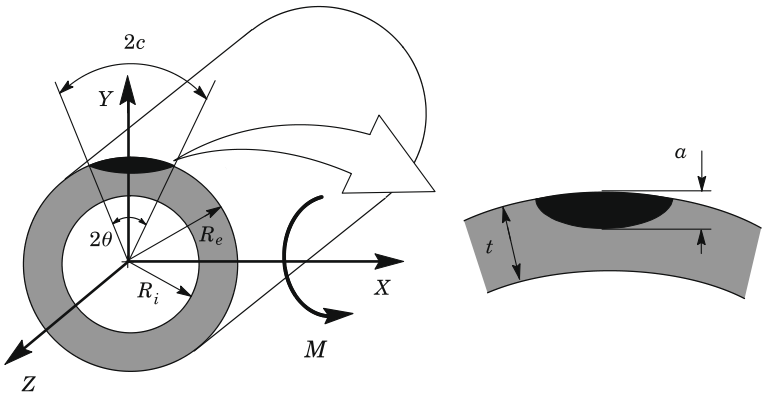


**Fig. 1.** Pipe configuration and defect geometry adopted in the numerical analyses.

where $D_e$ is the pipe (cylinder) outer diameter, $t$ is the wall thickness, $M$ denotes the applied bending moment and $M_0$ defines the limit bending moment. Here, the uncracked ligament is now given by $b = t - a$ and the surface crack length is described by the angle $\theta$ (see Fig. 1) as [10,19]

$$\theta = \frac{\pi c}{2D_e} \tag{13}$$

where $c$ is the circumferential crack half-length.

In the above expressions, the limit bending moment, $M_0$, is conventionally given by [10,19]

$$M_0 = 2\sigma_{ys}R_m^2 t(2\sin\beta - \frac{a}{t}\sin\theta) \tag{14}$$

in which $R_m$ denotes the mean radius ($R_m = (R_e + R_i)/2$ where $R_e$ and $R_i$ are the external and internal radius) and parameter $\beta$ is defined as

$$\beta = \frac{\pi}{2}\left[1 - \left(\frac{\theta}{\pi}\right)\left(\frac{a}{t}\right)\right] \tag{15}$$

The limit solution for the bending moment given by Eq. (14) is applicable in the range $(\theta + \beta) \leq \pi$ [10,19]. Other expressions for the limit bending moment could also be adopted to reflect more accurately the actual plastic collapse mechanism of the remaining crack ligament (see e.g. Chiodo and Ruggieri [26]). However, since $M_0$ in Eqs. (11) and (12) can be viewed just as a normalizing load which would affect only the values of factors $h_1$ and $h_2$ not the values of $J_p$ and $\delta_p$, this option was not pursued in the present work and should be addressed in future investigations.

Finally, the elastic terms of $J$ and CTOD, $J_e$ and $\delta_e$, are calculated by using Eqs. (6) and (9) coupled with a convenient form for the elastic stress intensity factor, $K_I$. For a circumferential surface crack in a pipe subjected to a bending moment, an improved expression for parameter $K_I$ is given by [10]

$$K_I = \sigma_b G_5 \sqrt{\frac{\pi a}{Q_s}} \tag{16}$$

where $\sigma_b$ is the (global or net-section) bending stress about the $x$-axis (see Fig. 1) expressed as

$$\sigma_b = \frac{4MR_e}{\pi(R_e^4 - R_i^4)} \tag{17}$$

and the flaw shape parameter, $Q_s$, is defined as

$$Q_s = 1 + 1.464\left(\frac{a}{c}\right)^{1.65}, \quad a \leqslant c. \tag{18}$$

In the above expression (16), $G_5$ is the influence coefficient corresponding to a circumferential semi-elliptical surface crack in a cylinder subjected to a (pure) net-section bending as given in Appendix C of API 579 [10].

Evaluation of parameters $J$ and CTOD based upon the procedure outlined above requires specification of factors $h_1$ and $h_2$ once all other quantities entering directly into the calculation of $J_e(\delta_e)$ and $J_p(\delta_p)$ are defined. Current available solutions (such as the EPRI methodology [16,19]) provide values for factor $h_1$ which are only applicable to few selected crack geometries, including circumferentially cracked pipes under axial load. The relatively limited analyses and data available to evaluate $J$ and CTOD for a broad range of crack geometries and material properties underscores the need for improved and accurate descriptions of factors $h_1$ and $h_2$ for circumferential surface cracks in pipes under bending. Section 4 explores detailed numerical and validation analyses which lead to a comprehensive body of fully-plastic solutions for $J$ and CTOD.

## 3. Computational procedures and finite element models

### 3.1. Numerical models of circumferentially cracked pipes

Nonlinear 3-D finite element analyses are conducted on circumferentially cracked pipes with external surface flaws subjected to bending. The analyzed pipe models have wall thickness $t$ = 20.6 mm with different outside diameters $D_e = 206\,\text{mm}$ $(D_e/t = 10), D_e = 309\,\text{mm}$ $(D_e/t = 15)$ *and* $D_e = 412\,\text{mm}$ $(D_e/t = 20)$. These geometries typify current trends in high pressure, high strength pipelines, including submarine pipelines and risers. The analysis matrix considers external surface flaws with varying crack depth ($a$) and crack length ($2c$) as defined by $a/t$ = 0.1–0.5 with increments of 0.05 and $\theta/\pi$ = 0.04, 0.08, 0.12, 0.16 and 0.20 ($1.7 \leqslant \{c/a\} \leqslant 82.5$ – see Eq. (13)). Fig. 1 shows the pipe configuration and defect geometry adopted in the analyses. Overall, the computations comprised 135 numerical models and 405 loading cases considering the three hardening levels adopted in the analyses (refer to Section 3.2 next).

Fig. 2a and b shows the finite element model constructed for the pipe with $D_e/t = 10, a/t = 0.5$ and $\theta/\pi = 0.12$. A conventional mesh configuration having a focused ring of elements surrounding the crack front is used with a small key-hole geometry (blunt tip) at the crack tip to enhance numerical convergence and to accommodate the large plastic strains that develop with increased levels of deformation. The small initial root radius at the crack tip is $\rho_0$ = 5 μm (0.005 mm). A typical half-symmetric model for the cracked pipes has approximately 15,000 elements and 18,000 nodes with appropriate constraints imposed on nodes defining the symmetry planes. The crack front is described by 15 (circumferential) layers defined over the crack half-length ($c$); the thickest layer is defined at the deepest point of the crack with thinner layers defined near the free surface to accommodate the strong gradient in the stress distribution along the crack front. The half-symmetric finite element models for the pipe specimens are loaded by a four-point bending scheme so that a constant bending moment with zero shear forces is imposed on the crack plane and along the pipe half-length at distances about three times the pipe diameter. Exploratory numerical analyses demonstrate that such loading scheme and associated boundary conditions, including the adopted pipe length, does not influence the near-tip stress and strain fields nor does it affect the $J$ and CTOD values extracted from the finite element computations. Very similar finite element models and mesh details are employed for other cracked pipe configurations.

3-D finite element analyses are also conducted on circumferentially cracked pipes subjected to reeling. Fig. 3 illustrates the adopted scheme for the numerical simulation of reeling with the reel drum being modeled by a rigid surface with diameter $\Phi_r$ = 15,000 mm; in the figure, Δ; represents the load line displacement (LLD). The pipe analyzed has an outside diameter, $D_e$ = 344.5 mm (13.5 in.), thickness, $t$ = 20.6 mm ($D_e/t \approx 16.7$) and external, circumferential surface flaws with length $2c$ = 100 mm ($\theta/\pi$ = 0.073) and different crack depth ($a$) over pipe wall thickness ($t$) ratios: $a/t$ = 0.1, 0.2, 0.3 and 0.4 (see Fig. 1). These geometries typify current trends in marine risers installed by the reeling process. Finite element models essentially similar as described above (but with a larger pipe length to accommodate pipe reeling over the drum) are employed for the reeling simulation. The half-symmetric models for these analyses have ~55,000 8-node, 3-D elements (~67,000 nodes) with appropriate constraints imposed on nodes defining the longitudinal symmetry plane.

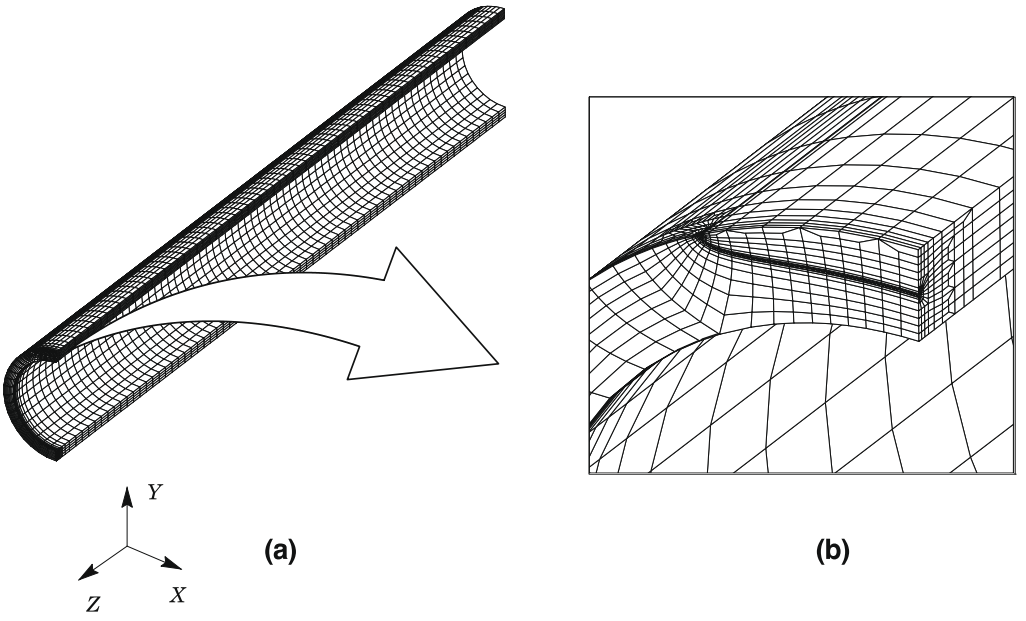


**Fig. 2.** (a) 3-D finite element model employed for the pipe configuration with $D_e/t$ = 10, $a/t$ = 0.5 and $\theta/\pi$ = 0.12 and (b) near-tip model and meshing details.

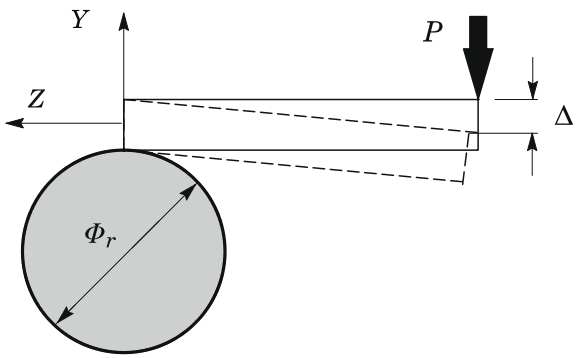


**Fig. 3.** Adopted scheme for the numerical simulation of pipe reeling.

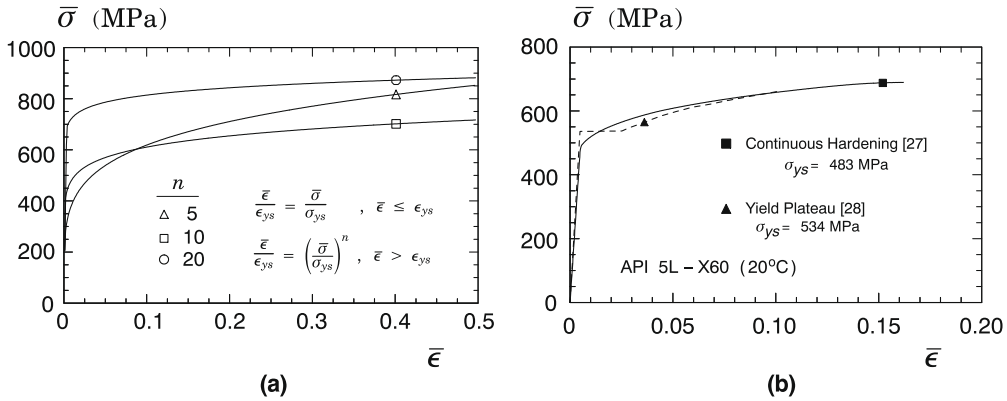


**Fig. 4.** (a) Uniaxial true stress–logarithmic strain response of materials employed in the analyses using a power-hardening model and (b) uniaxial true stress–logarithmic strain response for an API X60 steel having different hardening behavior after yielding.

### 3.2. Material models

The elastic–plastic constitutive model employed in all analyses reported here follows a $J_2$ flow theory with conventional Mises plasticity in small geometry change (SGC) setting. The numerical solutions employ a simple power-hardening model to characterize the uniaxial true stress ($\bar{\sigma}$) vs. logarithmic strain ($\bar{\varepsilon}$) in the form

$$\frac{\bar{\varepsilon}}{\varepsilon_{ys}} = \frac{\bar{\sigma}}{\sigma_{ys}} \quad \bar{\varepsilon} \le \varepsilon_{ys} \quad ; \quad \frac{\bar{\varepsilon}}{\varepsilon_{ys}} = \alpha\left(\frac{\bar{\sigma}}{\sigma_{ys}}\right)^n \quad \bar{\varepsilon} > \varepsilon_{ys} \tag{19}$$

where $\sigma_{ys}$ and $\varepsilon_{ys}$ are the (yield) stress and strain, $\alpha$ is a dimensionless constant and $n$ is the strain hardening exponent. The finite element analyses consider material flow properties covering typical structural, pressure vessel and pipeline grade steels with $E = 206$ GPa, $\nu = 0.3$ and $\alpha = 1$: $n = 5$ and $E/\sigma_{ys} = 800$ (high hardening material), $n = 10$ and $E/\sigma_{ys} = 500$ (moderate hardening material), $n = 20$ and $E/\sigma_{ys} = 300$ (low hardening material). These ranges of properties also reflect the upward trend in yield stress with the increase in strain hardening exponent, $n$, characteristic of ferritic structural steels, including pipeline steels. The stress–strain response for these materials is shown in Fig. 4a.

The evaluation procedure for factors $h_1$ and $h_2$ described in Section 4.2 requires specification of the ultimate tensile strength, $\sigma_{uts}$, to determine the level of $J$ (and CTOD) at which the limit bending moment corresponding to instability of the crack ligament for the pipe is attained. For each material property set, $\sigma_{uts}$ is estimated using the following relationship [5]

$$\sigma_{uts} = \sigma_{ys}\left[\frac{(500/n)^{1/n}}{\exp(1/n)}\right]. \tag{20}$$

Section 5 addresses a sensitivity analysis to assess the robustness of the $R$–$O$ power-law fit given by previous Eq. (1) in characterizing the crack-tip driving force as measured by $J$ (and, equivalently, CTOD). Section 6 describes numerical analyses for circumferentially cracked pipes subjected to reeling. The material adopted in these studies is a typical API 5L Grade X60 pipeline steel [36] but with two different true stress vs. true strain behavior after yielding as displayed in Fig. 4b. The solid line represents a pipeline steel with continuous hardening behavior having 483 MPa yield stress ($\sigma_{ys}$) at room temperature

(20 °C) and relatively low hardening properties ($\sigma_{uts}/\sigma_{ys} \approx 1.24$) tested by Silva [27]. The stress–strain data for this material was obtained using rectangular tensile specimens (ASTM A370 [37]) with 13 mm thickness (average of three tensile tests). Here, a conventional fitting of the true stress–true strain data to the *R–O* model provides $n = 12$ with $\alpha = 1$. The dashed line describes the true stress vs. true strain response for a pipeline steel displaying a Lüders plateau with yield stress, $\sigma_{ys} = 534$ MPa, also at room temperature given in Ref. [28]. The *R–O* power-law fitting for this data set using Eq. (1) gives $\alpha = 9.5$ and $n = 6.6$. Other mechanical properties for the material include Young's modulus, $E = 210$ GPa and Poisson's ratio, $\nu = 0.3$.

### 3.3. Computational procedures

The finite element code WARP3D [23] provides the numerical solutions for the 3-D analyses reported here. The code solves the equilibrium equations at each iteration using a very efficient, sparse matrix solver highly tuned for Unix and PC based architectures and implements the so-called $\overline{B}$ formulation [24] to preclude mesh lock-ups that arise as the deformation progresses into fully plastic, incompressible modes. The sparse solver significantly reduces both memory and CPU time required for solution of the linearized equations compared to conventional direct solvers.

The local value of the mechanical energy release rate at a point $s$ along the crack front is given by [25]

$$J = \int_{\Gamma} \left[ W_s n_1 - \sigma_{ij} \frac{\partial u_i}{\partial X_1} n_j \right] d\Gamma \tag{21}$$

where $\Gamma$ denotes a contour defined in a plane normal to the front on the undeformed configuration beginning at the bottom crack face and ending on the top face, $n_j$ is the outward normal to $\Gamma$, $W_s$ denotes the stress-work density per unit of undeformed volume, $\sigma_{ij}$ and $u_i$ are Cartesian components of stress and displacement in the crack front coordinate system. The finite element computations employ a domain integral procedure [25] for numerical evaluation of Eq. (21) to provide pointwise values of $J$ across the crack front at each loading level.

For the 3-D analyses of the circumferentially surface cracked pipes, the intensity of near-tip deformation is quantified by the pointwise value of $J$ evaluated at the point of maximum crack depth (see Figs. 1 and 2). Because the near-tip stress triaxiality is maintained over a large portion of the crack front [38] at the deepest point region and at distances sufficiently far from the traction-free (external) face of the pipe, such $J$-value adequately characterizes the level of crack-tip loading level needed in the estimation procedure for factor $h_1$ conducted next. Moreover, because of the relatively thin thickness of the analyzed pipes, additional care was taken to avoid having $J$ contours spreading towards the inner pipe surface which would thereby affect the path independence. In evaluating the path independent $J$-values for all numerical analyses, contours lying far from the crack tip but with a large enough size such as not to interact with the inner pipe surface were chosen. To determine the dimensionless function $h_2$, evaluation of the numerical values of CTOD follows the 90° intercept procedure [5] to the deformed crack flanks. To maintain consistency with the previous characterization of the intensity of near-tip deformation, the CTOD is also evaluated at the point of maximum crack depth. Our previous numerical experience reveals that such numerical technique to extract the CTOD in the analyzed crack configurations provides numerical values that differ by less than 10% of the displacement at the node of the initial crack tip while, at the same time, avoiding the evaluation of nodal displacements over a severely deformed region.

The numerical simulation of the reeling process involves the contact interaction between the pipe specimen and the reel drum represented by a rigid cylinder (see Fig. 3). WARP3D [23] uses a simple penalty method to enforce displacement constraints in the solution of the finite element model which creates springs at the contact points. The spring stiffness corresponds to the penalty parameter, while the amount of remaining penetration corresponds to the error in the enforcement of the constraint. The numerical procedure adds each spring stiffness into the corresponding element stiffness matrices instead of directly into the global stiffness matrix.

## 4. *J* and CTOD estimation based on the *h*-factors

The following sections provide an extensive set of results derived from the 3-D numerical analyses conducted on circumferentially cracked pipes with varying crack configuration under bending. These results include factors $h_1$ and $h_2$ needed to determine $J$ and CTOD for a given measure of applied (macroscopic) loading as characterized by the bending moment in the present context. The analyses also explore key issues of the evaluation procedure for factor $h_1$ (the procedure to evaluate factor $h_2$ is essentially similar) which have a direct bearing on the robustness of the fully plastic solutions to estimate $J$ and CTOD for circumferentially cracked pipes. These issues include the sensitivity of factor $h_1$ (and, equivalently, factor $h_2$) on crack-tip loading coupled with geometry and strain hardening effects.

### 4.1. Dependence of factor $h_1$ on crack-tip loading

The present framework to support the use of the dimensionless functions $h_1$ in the estimation procedure for $J$ defined by Eq. (11) holds true as long as the proportional relationship between the applied loading ($M$) and $J_p$ given by previous Eq. (11) is preserved with increased levels of crack-tip loading. Consequently, the key question to resolve with the $J$ evaluation

procedure for a circumferentially cracked pipe concerns the sensitivity of the condition $J_p \propto (M/M_0)^{n+1}$ on loading level changes for a given crack configuration.

Figs. 5a and b and 6a and b provide the variation of $\log J_p$ with $\log (M/M_0)$ for selected pipe geometries using crack configurations and material properties with widely different behavior in crack tip constraint and strain hardening. These analyses cover pipe specimens with $D_e/t = 10$ and 20, $a/t = 0.2$ and 0.5, $\theta/\pi = 0.04$ and 0.20 with two hardening levels, $n = 5$ and 20. In these plots, a reference line with slope $n + 1$ is provided to aid in assessing the constant ratio (proportionality) between $\log J_p$ and $\log (M/M_0)$. Further, the particular point given by $\log (M/M_0) = 0$ (which corresponds to $M = M_0$) has a clear interpretation as it corresponds to the attainment of the limit bending moment (as defined by Eq. (14)) for each analyzed configuration.

Consider first the results for the pipe specimens with $D_e/t = 10$ and $n = 5$ displayed in Fig. 5a and b. Each curve for a specific $a/t$ and $\theta/\pi$-ratio follows very closely the corresponding reference line which defines the constant ratio between $\log J_p$ and $\log (M/M_0)$, particularly for applied bending moments exceeding the limit bending moment. Here, after the well contained, near-tip elastic–plastic stress fields evolve into a fully plastic condition (in which the crack ligament has reached yielding), the variation of $\log J_p$ with $\log (M/M_0)$ essentially falls onto the reference line thereby translating into a constant ratio. Consider next the results for the pipe specimens with $D_e/t = 20$ and $n = 20$ displayed in Fig. 6a and b. While a relatively linear dependence of $\log J_p$ on $\log (M/M_0)$ is still preserved for the shallow ($a/t = 0.2$) and deeply ($a/t = 0.5$) cracked pipe specimens with $\theta/\pi = 0.04$ at values of the applied bending moment corresponding to $\log(M/M_0) \geq 0.03 \sim 0.05$, the variation of $\log J_p$ with $\log (M/M_0)$ for the $\theta/\pi = 0.20$ configuration deviates significantly from the proportionality reference line particularly for the pipe specimen with $a/t = 0.5$. This behavior exhibited by the $n = 20$ material contrasts rather sharply with the features observed for the $n = 5$ material and poses additional difficulties in the procedure to extract factor $h_1$ as discussed next. Although not shown here in interest of space, essentially similar trends are also observed for the dependence of factor $h_2$ with CTOD for the analyzed pipe configurations.

### 4.2. Evaluation procedure of factor $h_1$ and $h_2$

Evaluation of factor $h_1$ and $h_2$ for the analyzed crack configurations follows from solving Eqs. (11) and (12) upon computation of the plastic component of the $J$-integral, $J_p$, and CTOD, $\delta_p$, with the applied bending moment, $M$, for a given crack size, component geometry and strain hardening exponent, $n$. Based upon the previous results and to develop a more consistent scheme to determine the dimensionless function $h_1$ (the process to evaluate factor $h_2$ is analogous), it proves convenient to rewrite Eq. (11) into the form

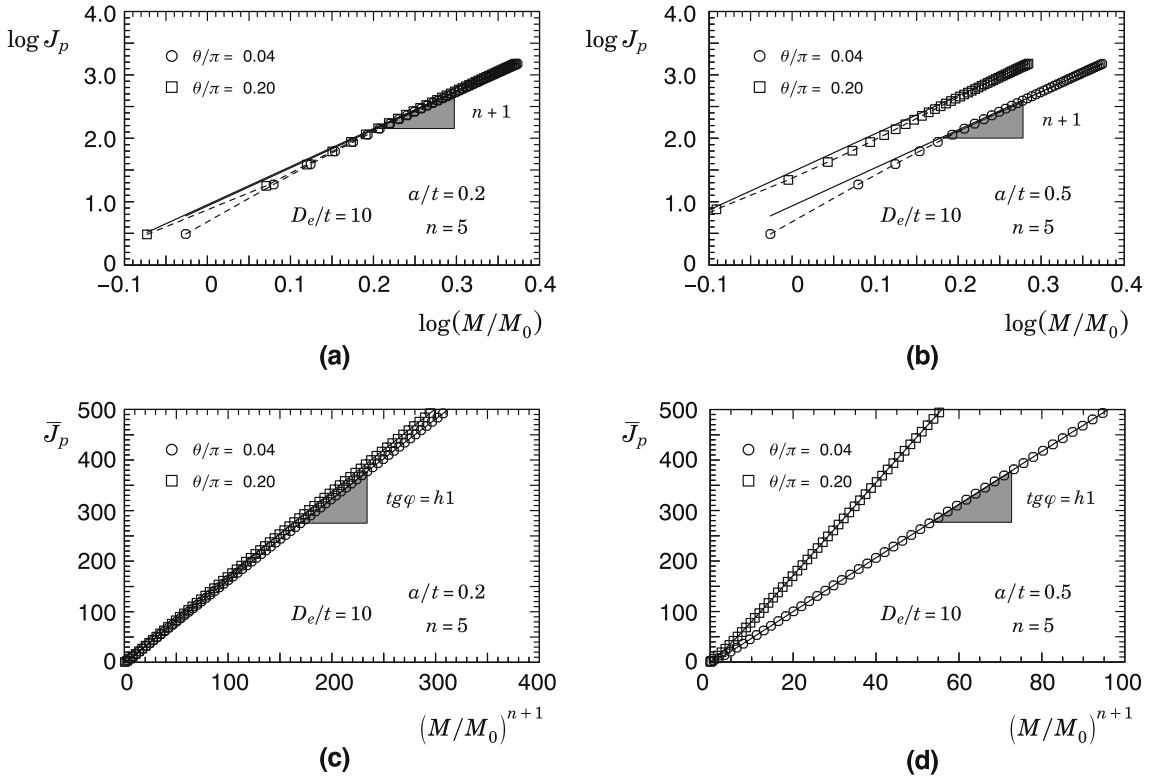


**Fig. 5.** Variation of the $J$-integral with increased normalized bending moment for the pipe configuration with $D_e/t = 10$, $n = 5$ material and varying crack configuration.

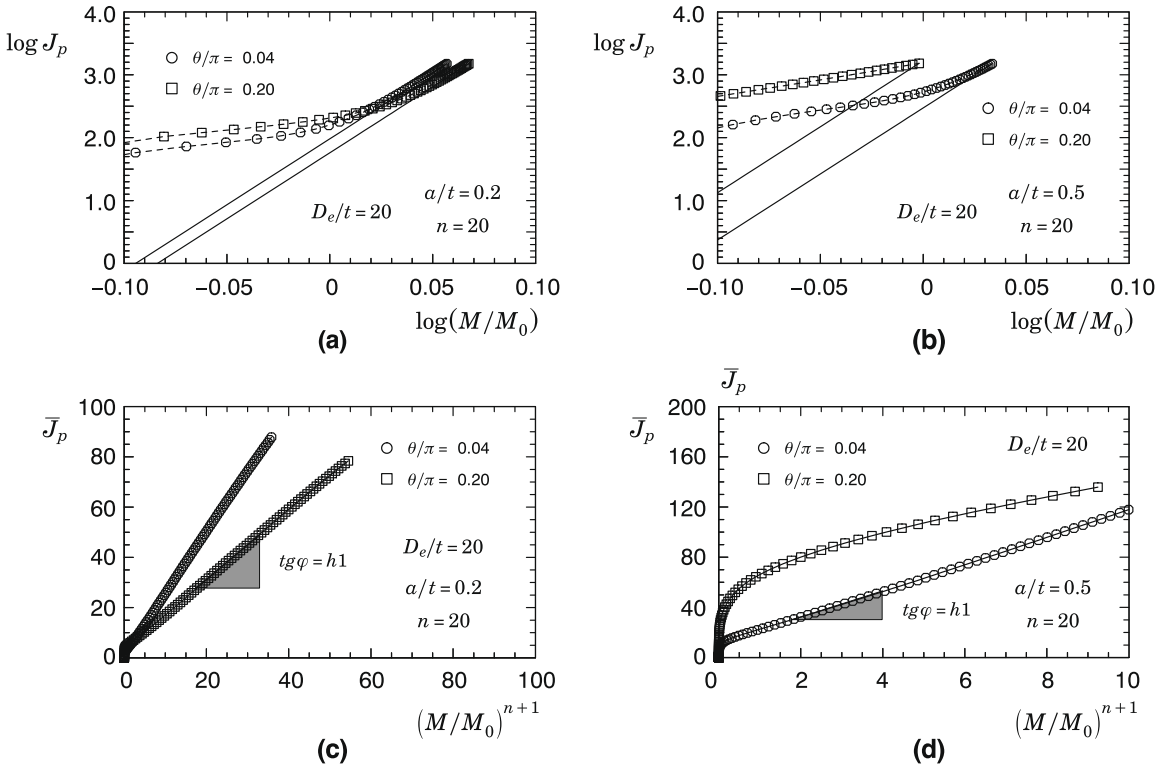


**Fig. 6.** Variation of the $J$-integral with increased normalized bending moment for the pipe configuration with $D_e/t = 20$, $n = 20$ material and varying crack configuration.

$$\bar{J}_p = \frac{J_p}{\alpha \varepsilon_{ys} \sigma_{ys} b} = h_1(a/t, D_e/t, \theta, n)\left(\frac{M}{M_0}\right)^{n+1} \tag{22}$$

so that factor $h_1$ can be obtained by simply determining the slope of a least square fit to the (linear) evolution of $\bar{J}_p$ with $(M/M_0)^{n+1}$.

Figs. 5c and d and 6c and d illustrates the procedure to determine factor $h_1$ for the circumferentially cracked pipes analyzed in the previous section. First, direct attention to the results for the pipe specimens with $D_e/t = 10$ and high strain hardening ($n = 5$) material displayed in Fig. 5c and d. For all analyzed cases covering widely different crack geometries as characterized by the $a/t$ and $\theta/\pi$-ratio, a linear relationship between $\bar{J}_p$ and $(M/M_0)^{n+1}$ clearly holds true for the entire range of load level. Here, the slope of the straight line derived from the best fit to the computed values unmistakably defines factor $h_1$ for a given crack configuration. Consider now the results for the pipe specimens with $D_e/t = 20$ and low strain hardening ($n = 20$) material displayed in Fig. 6c and d. Because the variation of $\log J_p$ with $\log(M/M_0)$ at load levels $M < M_0$ ($\log(M/M_0) < 0$) deviates significantly from a linear function (see Fig. 6a and b), the early portion of the two sets of curves potentially display dramatic changes in slope thereby complicating the assessment of a "correct" value for factor $h_1$ by a best fit procedure. Neglecting this short transient region, which corresponds to applied load levels (here characterized by the bending moment) that are not relevant in describing fully plastic stress states, may eliminate this problem for the short crack pipe ($a/t = 0.2$) but not for the full range of crack geometries for deeply cracked pipes ($a/t \geq 0.3$—$0.4$). Indeed, while it is still possible to define factor $h_1$ for the deeply cracked pipe within reasonable accuracy for $\theta/\pi = 0.04$, a representative value of $h_1$ for $\theta/\pi = 0.20$ remains undefined. Moreover, for very large deformation levels near the plastic collapse load of the cracked pipe, failure is generally governed by the flow properties of the material, particularly its tensile stress ($\sigma_{uts}$), not by the fracture toughness. Chiodo and Ruggieri [26] discuss this issue in detail and provide limit load solutions for axially cracked pipes which have a direct bearing on the discussion pursued here. Consequently, defining factor $h_1$ as the slope of the (best fit) straight line corresponding to the late part of the $\bar{J}_p$ vs. $(M/M_0)^{n+1}$ curve for some combinations of crack configurations and material properties remains elusive.

To address this issue and to provide a simpler evaluation procedure for factor $h_1$ (and, equivalently, factor $h_2$) applicable to a wide range of crack configurations and material properties, the present investigation adopts the following scheme:

(1) Determine the $J$-value corresponding to the limit bending moment evaluated from Eq. (14) using the material's yield stress, $\sigma_{ys}$. Let $J_y$ denote this crack-tip loading level.

(2) Determine the $J$-value corresponding to the limit bending moment evaluated from Eq. (14) but with the yield stress, $\sigma_{ys}$, replaced by the (ultimate) tensile stress, $\sigma_{uts}$. Let $J_t$ denote this crack-tip loading level.
(3) For the $J$-values ranging from $J_y$ to $J_t$, determine the corresponding plastic component, $J_p$.
(4) Plot $\bar{J}_p$ vs. $(M/M_0)^{n+1}$ for the $J$-values ranging from $J_y$ to $J_t$ and evaluate factor $h_1$ as the slope of the best fit straight line passing through the axis origin for the selected range of crack-tip loading.

The above strategy maintains consistency with the linear relationship condition between $\bar{J}_p$ and $(M/M_0)^{n+1}$ while avoiding considering unrealistically high levels of crack-tip loading (as characterized by $J$-values larger than $J_t$) which would otherwise enter into the linear fitting scheme. This scheme also applies when the CTOD is employed to characterize the crack-tip driving force; here, the corresponding quantities entering the process are $\delta_p$, $\bar{\delta}_p$, $\delta_y$ and $\delta_t$. However, the evaluation procedure for factor $h_1$ (and factor $h_2$) is applicable only to the extent that a sufficiently valid range of $J$-values (CTOD-values) follow a proportional relationship with the applied loading ($M$). The numerical results reported subsequently reveal a few cases for which the evaluation of factor $h_1$ (and factor $h_2$) becomes unacceptably inaccurate.

### 4.3. Factors $h_1$ for circumferential surface cracks in pipes under bending

Figs. 7–9 provide the $h_1$-factors for the circumferentially cracked pipes with varying geometries and material properties derived from the $J$ estimation procedure previously outlined. For all sets of analyses, the results reveal that factor $h_1$ displays a rather strong sensitivity to crack geometry and strain hardening behavior. To facilitate interpretation of these results, direct first attention to a fixed $D_e/t$-ratio such as the plots for $D_e/t = 10$ displayed in Fig. 7. For shallow crack sizes ($a/t < 0.2$—$0.3$), the $h_1$-values are fairly insensitive to crack length (defined by parameter $\theta/\pi$) for all hardening levels; here, the evolution of factor $h_1$ with crack depth essentially falls onto a single curve particularly for $a/t < 0.2$. In contrast, the $h_1$-factors for deeply cracked pipes ($a/t > 0.4$) depend rather strongly on $\theta/\pi$ for all hardening levels, particularly for shorter crack lengths ($\theta/\pi \leq 0.12$). Very similar trends are displayed by other $D_e/t$-ratios – see Figs. 8 and 9.

Further, we note that the evolution of factor $h_1$ with $\theta/\pi$ for a fixed $a/t$-ratio displays a somewhat mixed behavior as it increases and then slightly decreases with increased $\theta/\pi$-values. Such development is particularly prominent in the deep crack range ($a/t > 0.4$) for all hardening levels. Consider, for example, the $h_1$-values for $n = 10$ and $a/t = 0.5$ displayed in Fig. 7b; here, factor $h_1$ changes rapidly from $\theta/\pi = 0.04$ to $\theta/\pi = 0.08$ and then exhibits a slight drop from the peak level attained at $\theta/\pi = 0.12$ with increased crack length. We argue that these trends in variation of factor $h_1$ are associated with the synergistic combination of crack depth (which defines the crack ligament size) and circumferential crack length. Such synergism potentially impacts the evolution of the highly-strained plastic zones along the crack ligament with increased

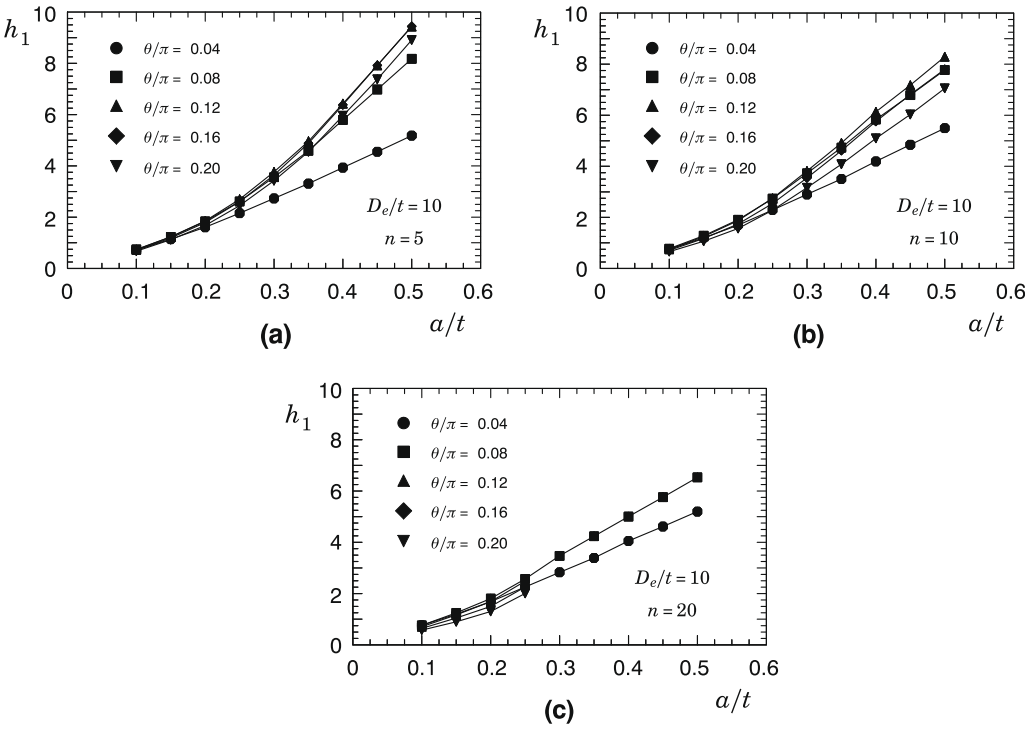


**Fig. 7.** Variation of factor $h_1$ with increased $a/t$-ratio for the pipe configuration with $D_e/t = 10$ and varying circumferential crack length and hardening properties.

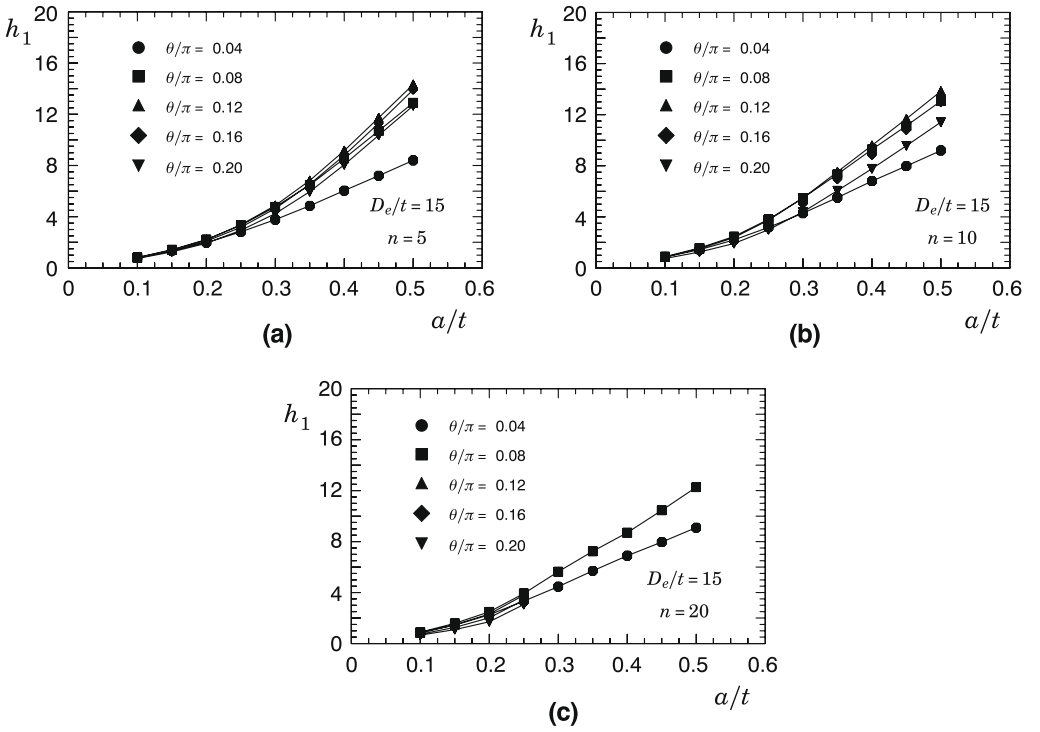


**Fig. 8.** Variation of factor $h_1$ with increased $a/t$-ratio for the pipe configuration with $D_e/t = 15$ and varying circumferential crack length and hardening properties.

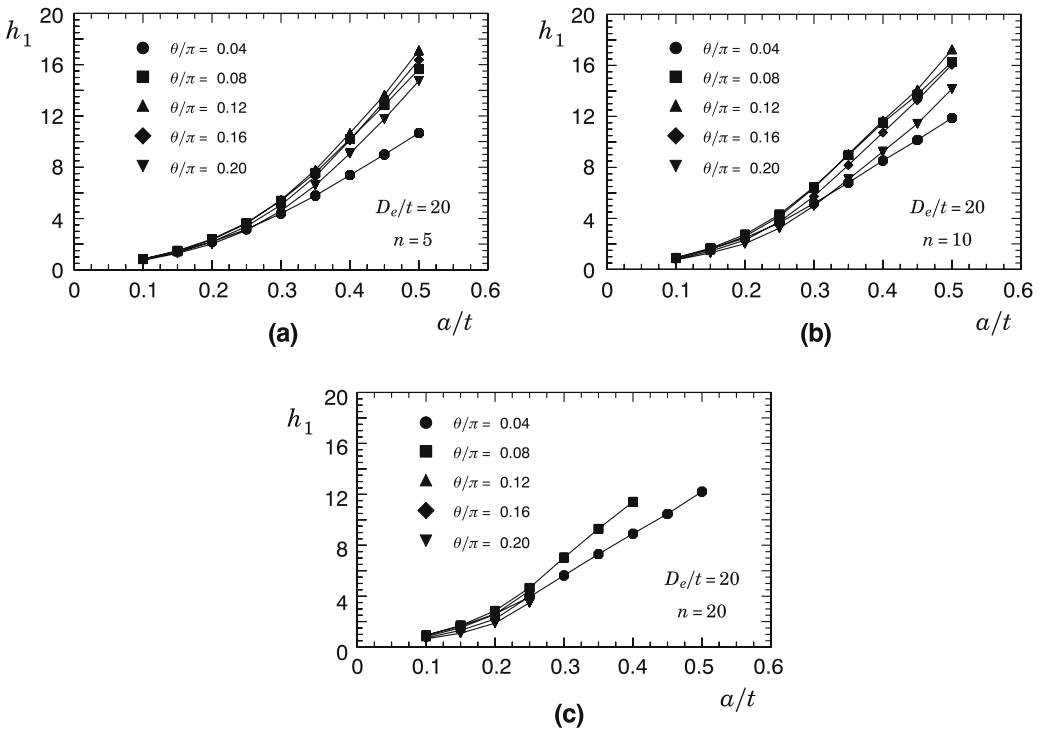


**Fig. 9.** Variation of factor $h_1$ with increased $a/t$-ratio for the pipe configuration with $D_e/t = 20$ and varying circumferential crack length and hardening properties.

**Table 1**
Coefficients for the polynomial fitting of factor $h_1$ given by Eq. (23) for $D_e/t = 10$.

| $D_e/t$ | $n$ | $\theta/\pi$ | $\xi_0$ | $\xi_1$ | $\xi_2$ | $\xi_3$ |
|---|---|---|---|---|---|---|
| 10 | 5 | 0.04 | 0.0843 | 4.6422 | 17.8277 | −13.4842 |
| | | 0.08 | 0.5825 | −3.3878 | 55.2778 | −36.1407 |
| | | 0.12 | 0.7313 | −5.6312 | 62.2795 | −32.1912 |
| | | 0.16 | 0.8515 | −7.2849 | 65.8250 | −33.4485 |
| | | 0.20 | 0.6612 | −4.6699 | 52.5089 | −20.1966 |
| | 10 | 0.04 | 0.1164 | 4.3912 | 21.2600 | −17.0781 |
| | | 0.08 | 0.7107 | −5.7907 | 72.0217 | −64.4680 |
| | | 0.12 | 0.8698 | −8.6330 | 83.1300 | −72.4532 |
| | | 0.16 | 0.9889 | −10.2750 | 85.1026 | −74.5791 |
| | | 0.20 | 0.6988 | −5.9989 | 61.9058 | −49.0822 |
| | 20 | 0.04 | 0.1271 | 4.4459 | 20.7199 | −18.6707 |
| | | 0.08 | 0.3441 | −0.4818 | 50.1959 | −49.2222 |
| | | 0.12[a] | 0.3936 | −1.7114 | 51.8556 | −45.3296 |
| | | 0.16[a] | 0.6379 | −5.3930 | 59.8801 | −49.3589 |
| | | 0.20[a] | 0.9254 | −10.1875 | 74.3664 | −64.2550 |

[a] Note: valid in the range $a/t < 0.25$.

**Table 2**
Coefficients for the polynomial fitting of factor $h_1$ given by Eq. (23) for $D_e/t = 15$.

| $D_e/t$ | $n$ | $\theta/\pi$ | $\xi_0$ | $\xi_1$ | $\xi_2$ | $\xi_3$ |
|---|---|---|---|---|---|---|
| 15 | 5 | 0.04 | 0.5223 | −2.2280 | 55.3610 | −38.7590 |
| | | 0.08 | 1.1077 | −11.0849 | 91.1526 | −43.3009 |
| | | 0.12 | 1.2639 | −13.1859 | 94.3227 | −30.8805 |
| | | 0.16 | 1.2108 | −12.2124 | 86.0012 | −21.0857 |
| | | 0.20 | 1.2108 | −12.1170 | 82.1175 | −23.5905 |
| | 10 | 0.04 | 0.7285 | −5.8292 | 79.4549 | −67.9468 |
| | | 0.08 | 1.4662 | −18.2720 | 139.5870 | −113.4380 |
| | | 0.12 | 1.6937 | −21.8850 | 150.0590 | −115.5130 |
| | | 0.16 | 1.5520 | −19.4931 | 132.5110 | −95.9746 |
| | | 0.20 | 1.4883 | −17.9780 | 117.5820 | −83.8422 |
| | 20 | 0.04 | 0.7249 | −6.4982 | 88.3854 | −84.1349 |
| | | 0.08 | 0.6796 | −8.1227 | 107.3920 | −90.2424 |
| | | 0.12[a] | 0.7269 | −8.7736 | 99.7509 | −62.0301 |
| | | 0.16[a] | 1.2752 | −16.7803 | 120.3940 | −74.7073 |
| | | 0.20[a] | 2.0061 | −27.2343 | 151.7440 | −104.4900 |

[a] Note: valid in the range $a/t < 0.25$.

crack-tip loading thereby affecting the proportional relationship between $\bar{J}_p$ and $(M/M_0)^{n+1}$ upon which $h_1$ is defined – see Figs. 5 and 6.

The results for the $h_1$-values corresponding to the low hardening material ($n = 20$) shown in the plots of Figs. 7–9 also deserve attention. As we have previously discussed, factor $h_1$ is evaluated using a range of $J$-values in which they follow a proportional relationship with the applied bending moment, $M$. While this condition is met for the full range of $a/t$-values and $\theta/\pi = 0.04$, 0.08 for all $D_e/t$-ratios, the $h_1$ evaluation procedure for some combinations of crack depth ($a/t$) and crack length ($\theta/\pi$) for the $n = 20$ material fails to provide sufficiently accurate values. For $a/t$-ratios up through ~0.25, however, a full set of $h_1$-factors for the low hardening material and varying $D_e/t$-ratios is readily defined.

Using now the plots displayed in Figs. 7–9 for guidance and to provide a simpler manipulation of the previous results, we construct the functional dependence of factor $h_1$ and crack depth for a given $\theta/\pi$-ratio in the form

$$h_1(a/t) = \xi_0 + \xi_1(a/t) + \xi_2(a/t)^2 + \xi_3(a/t)^3 \tag{23}$$

where it is understood that a cubic polynomial fitting is employed. Tables 1–3 provide the polynomial coefficients of Eq. (23) derived from a standard least square fitting using the $h_1$ data set for each $D_e/t$ and $\theta/\pi$. For all $D_e/t$-ratios with $n = 20$ (low hardening material), the functional dependence between factor $h_1$ and crack depth for $\theta/\pi \geq 0.12$ given by Eq. (23) and the corresponding polynomial coefficients is strictly valid for $a/t \leq 0.25$ .

### 4.4. Factors $h_2$ for circumferential surface cracks in pipes under bending

Figs. 10–12 present the $h_2$-factors for the circumferentially cracked pipes with varying geometries and material properties which follow from the CTOD estimation procedure described in Section 4.2. As already noted, the connection of $J$ with CTOD

**Table 3**
Coefficients for the polynomial fitting of factor $h_1$ given by Eq. (23) for $D_e/t = 20$.

| $D_e/t$ | $n$ | $\theta/\pi$ | $\xi_0$ | $\xi_1$ | $\xi_2$ | $\xi_3$ |
|---|---|---|---|---|---|---|
| 20 | 5 | 0.04 | 0.7804 | −6.2095 | 74.4567 | −44.8433 |
| | | 0.08 | 1.6133 | −18.7368 | 123.2110 | −58.7412 |
| | | 0.12 | 1.5054 | −16.5979 | 106.4300 | −21.3341 |
| | | 0.16 | 1.5593 | −17.0274 | 101.9440 | −16.5603 |
| | | 0.20 | 1.2791 | −12.8952 | 82.3299 | −4.9121 |
| | 10 | 0.04 | 1.1411 | −12.5254 | 114.3470 | −92.8150 |
| | | 0.08 | 2.3246 | −32.3329 | 205.6480 | −170.6350 |
| | | 0.12 | 2.2216 | −30.7086 | 190.8510 | −139.3350 |
| | | 0.16 | 2.3225 | −31.3947 | 181.8030 | −128.1330 |
| | | 0.20 | 1.6794 | −21.2747 | 131.0190 | −77.5143 |
| | 20 | 0.04 | 0.9983 | −11.7835 | 122.3060 | −108.3160 |
| | | 0.08 | 1.4206 | −21.4716 | 176.6020 | −149.5850 |
| | | 0.12[a] | 1.3616 | −20.3624 | 156.4870 | −97.4329 |
| | | 0.16[a] | 2.6916 | −39.0150 | 214.3200 | −146.6190 |
| | | 0.20[a] | 2.6736 | −37.9678 | 193.0660 | −108.3540 |

[a] Note: valid in the range $a/t < 0.25$.

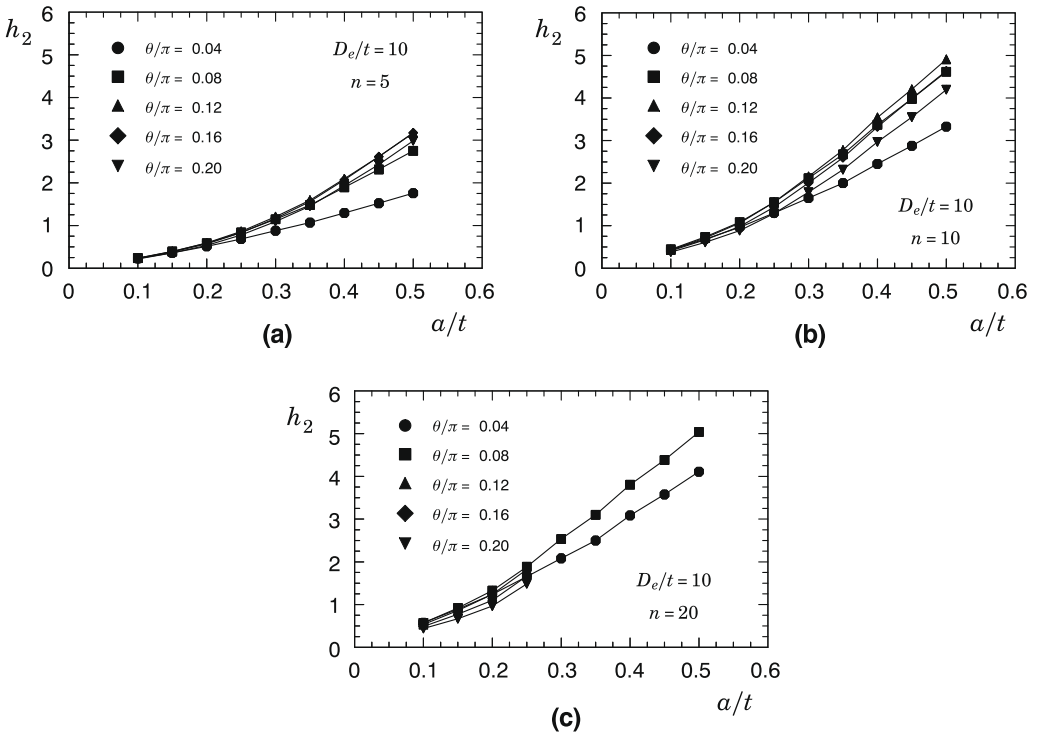


**Fig. 10.** Variation of factor $h_2$ with increased $a/t$-ratio for the pipe configuration with $D_e/t = 10$ and varying circumferential crack length and hardening properties.

given by Eq. (7) implies a linear relationship between factor $h_2$ and $h_1$ such that $h_2 = d_n h_1$. Consequently, much of the features and conclusions arising from the preceding results remain essentially similar for the $h_2$ results. Indeed, the trends are clear as factor $h_2$ is fairly independent of crack length (defined by parameter $\theta/\pi$) for shallower crack sizes ($a/t < 0.2$—$0.3$) but depends more sensitively on $\theta/\pi$ for deeper crack sizes ($a/t > 0.4$). Such trends are nearly the same for all hardening levels and $D_e/t$-ratios adopted in the analyses.

The behavior exhibited by the $h_2$-values for the low hardening material ($n = 20$) displayed in the plots of Figs. 10–12 is also consistent with the previous observations about the loss of proportionality between the crack-tip driving force (here characterized by the CTOD) and the applied bending moment, $M$, for some combinations of crack depth ($a/t$) and crack length ($\theta/\pi$). Again, a full set of $h_2$-factors for the low hardening material and varying $D_e/t$-ratios is readily defined only for $a/t$-ratios up through ~0.25.

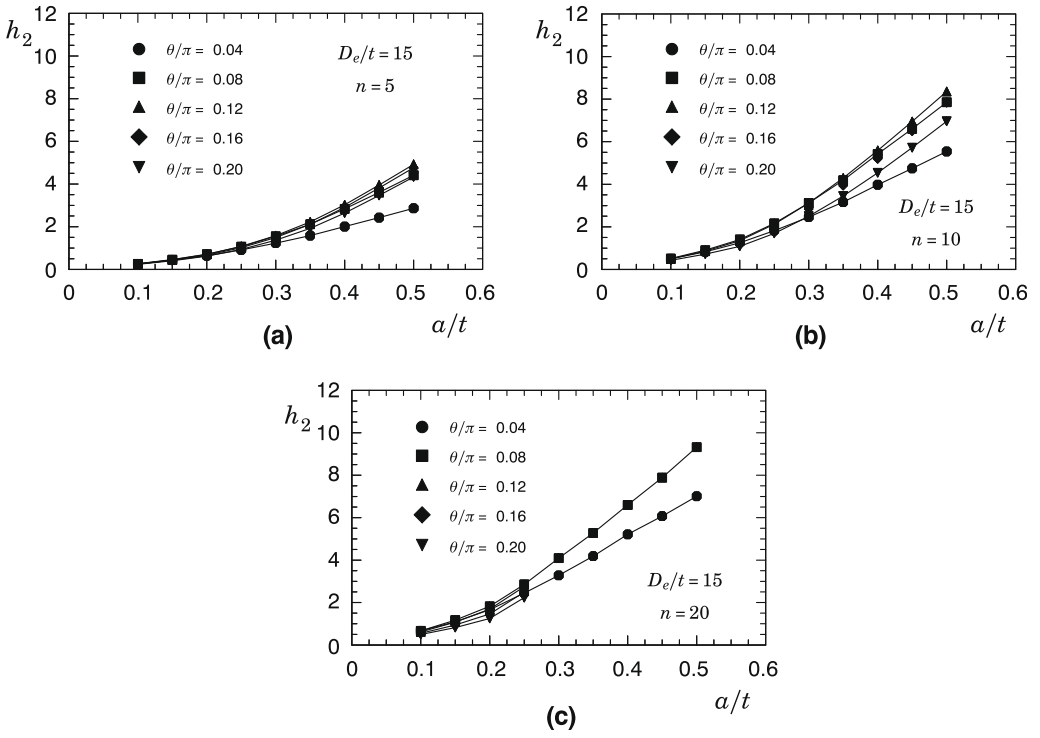


**Fig. 11.** Variation of factor $h_2$ with increased $a/t$-ratio for the pipe configuration with $D_e/t = 15$ and varying circumferential crack length and hardening properties.

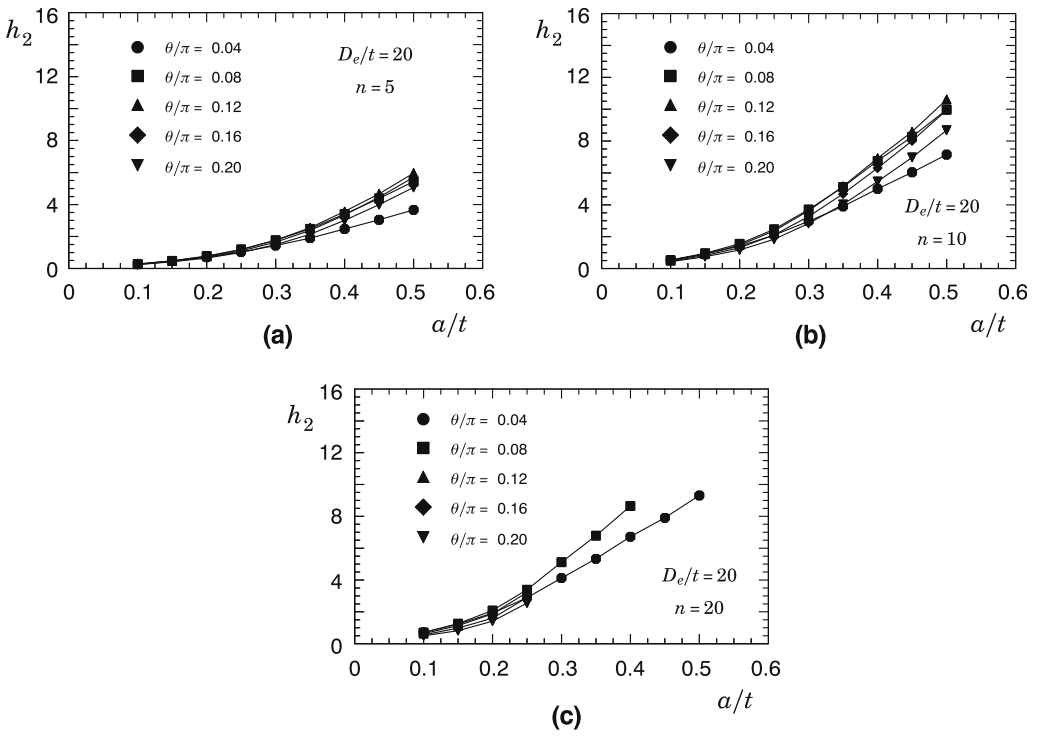


**Fig. 12.** Variation of factor $h_2$ with increased $a/t$-ratio for the pipe configuration with $D_e/t = 20$ and varying circumferential crack length and hardening properties.

**Table 4**
Coefficients for the polynomial fitting of factor $h_2$ given by Eq. (24) for $D_e/t = 10$.

| $D_e/t$ | $n$ | $\theta/\pi$ | $\xi_0$ | $\xi_1$ | $\xi_2$ | $\xi_3$ |
|---|---|---|---|---|---|---|
| 10 | 5 | 0.04 | 0.0354 | 1.4033 | 5.4291 | −2.7044 |
| | | 0.08 | 0.1667 | −0.7045 | 15.3951 | −7.2653 |
| | | 0.12 | 0.1934 | −1.1052 | 16.1908 | −4.1226 |
| | | 0.16 | 0.2191 | −1.4169 | 16.2839 | −3.1744 |
| | | 0.20 | 0.1770 | −0.8440 | 13.1158 | −0.3502 |
| | 10 | 0.04 | 0.0608 | 2.8476 | 9.1343 | −3.4923 |
| | | 0.08 | 0.3782 | −2.5864 | 36.3163 | −28.3582 |
| | | 0.12 | 0.4899 | −4.4918 | 43.5806 | −33.8202 |
| | | 0.16 | 0.5295 | −5.0153 | 43.0069 | −32.9966 |
| | | 0.20 | 0.4297 | −3.5362 | 33.9026 | −23.5226 |
| | 20 | 0.04 | 0.1243 | 3.3741 | 12.2899 | −6.1320 |
| | | 0.08 | 0.3301 | −0.9833 | 37.0877 | −32.6909 |
| | | 0.12[a] | 0.4404 | −3.0139 | 43.1056 | −35.5939 |
| | | 0.16[a] | 0.5508 | −4.8088 | 45.8284 | −35.2813 |
| | | 0.20[a] | 0.8679 | −9.9315 | 63.7080 | −55.5670 |

[a] Note: valid in the range $a/t < 0.25$.

**Table 5**
Coefficients for the polynomial fitting of of factor $h_2$ given by Eq. (24) for $D_e/t = 15$.

| $D_e/t$ | $n$ | $\theta/\pi$ | $\xi_0$ | $\xi_1$ | $\xi_2$ | $\xi_3$ |
|---|---|---|---|---|---|---|
| 15 | 5 | 0.04 | 0.1571 | −0.4836 | 16.2303 | −8.8411 |
| | | 0.08 | 0.3377 | −3.1063 | 25.9833 | −6.8249 |
| | | 0.12 | 0.3356 | −2.9458 | 23.2126 | 2.2170 |
| | | 0.16 | 0.3381 | −2.9094 | 21.5826 | 4.0762 |
| | | 0.20 | 0.3011 | −2.3603 | 18.4601 | 4.9386 |
| | 10 | 0.04 | 0.3929 | −2.6395 | 40.6976 | −29.6426 |
| | | 0.08 | 0.8111 | −9.5261 | 72.8777 | −51.2798 |
| | | 0.12 | 0.9035 | −10.9330 | 75.5084 | −47.5897 |
| | | 0.16 | 0.9281 | −11.0804 | 71.3802 | −43.0552 |
| | | 0.20 | 0.7636 | −8.4305 | 56.1487 | −28.9347 |
| | 20 | 0.04 | 0.5804 | −4.6881 | 61.6135 | −53.1298 |
| | | 0.08 | 0.6952 | −8.0026 | 83.2217 | −65.7404 |
| | | 0.12[a] | 0.7389 | −8.7522 | 79.0689 | −47.0087 |
| | | 0.16[a] | 1.3412 | −17.5454 | 106.3570 | −70.6527 |
| | | 0.20[a] | 1.6490 | −22.0627 | 117.7130 | −80.2001 |

[a] Note: valid in the range $a/t < 0.25$.

To provide a simpler manipulation of the results displayed in Figs. 10–12, a functional dependence of factor $h_2$ and crack depth for a given $\theta/\pi$-ratio is expressed in the form

$$h_2(a/t) = \zeta_0 + \zeta_1(a/t) + \zeta_2(a/t)^2 + \zeta_3(a/t)^3 \tag{24}$$

where a cubic polynomial fitting is utilized. Tables 4–6 provide the polynomial coefficients of Eq. (24) resulting from a standard least square fitting to the $h_2$ data set for each $D_e/t$ and $\theta/\pi$. As noted previously, the functional dependence between factor $h_2$ and crack depth for $\theta/\pi \geq 0.12$ given by Eq. (24) and the corresponding polynomial coefficients is strictly valid for $a/t \leqslant 0.25$ in the case of all $D_e/t$-ratios with $n = 20$ (low hardening material).

We now proceed to demonstrate that the relationship between $J$ and CTOD given by previous Eq. (7) holds true for the crack configurations under analysis such that $h_2 = d_n h_1$. Fig. 13 shows $d_n$-values for key selected crack configurations having varying $a/t$ and $\theta/\pi$-ratios with widely different hardening behavior ($n = 5$ and 20); these results are derived directly from the analyses previously presented to determine factors $h_1$ and $h_2$. The trends are clear. The resulting $d_n$-values are a strong function of the material's strain hardening (as characterized by the hardening exponent, $n$) and essentially independent of crack geometry and pipe diameter. Here, $d_n \approx 0.32$ for the high hardening material ($n = 5$) and $d_n \approx 0.75$ for the low hardening material ($n = 20$). For comparison, these constant (average) values are shown in the plots as dashed lines. Small departures from the constant line corresponding to $d_n \approx 0.75$ for the $n = 20$ material can be observed which is most likely associated with the fully plastic behavior and the relative difficulty in assessing very accurate values of factors $h_1$ and $h_2$ for this material (see Sections 4.1 and 4.2). However, these results fully confirm the applicability of the equivalence between $J$ and CTOD for the analyzed crack configurations.

**Table 6**
Coefficients for the polynomial fitting of of factor $h_2$ given by Eq. (24) for $D_e/t = 20$.

| $D_e/t$ | $n$ | $\theta/\pi$ | $\xi_0$ | $\xi_1$ | $\xi_2$ | $\xi_3$ |
|---|---|---|---|---|---|---|
| 20 | 5 | 0.04 | 0.2325 | −1.6216 | 21.6025 | −9.2529 |
| | | 0.08 | 0.4366 | −4.5415 | 31.5916 | −4.8595 |
| | | 0.12 | 0.3857 | −3.5337 | 24.3112 | 10.2439 |
| | | 0.16 | 0.3287 | −2.6519 | 18.9737 | 15.8038 |
| | | 0.20 | 0.3276 | −2.6404 | 18.3557 | 11.9382 |
| | 10 | 0.04 | 0.6073 | −6.1169 | 58.9117 | −40.9894 |
| | | 0.08 | 1.2300 | −16.2302 | 103.4560 | −72.0608 |
| | | 0.12 | 1.2549 | −16.3857 | 98.3200 | −56.3578 |
| | | 0.16 | 1.1391 | −14.3309 | 83.5881 | −39.3918 |
| | | 0.20 | 0.9393 | −11.0280 | 65.4325 | −24.7345 |
| | 20 | 0.04 | 0.8002 | −8.8741 | 87.5153 | −71.7065 |
| | | 0.08 | 1.2524 | −17.6992 | 131.8520 | −103.7140 |
| | | 0.12[a] | 1.5058 | −21.2431 | 134.6470 | −85.3270 |
| | | 0.16[a] | 2.2105 | −31.1656 | 162.8490 | −105.9320 |
| | | 0.20[a] | 2.4676 | −34.4221 | 165.0030 | −100.5140 |

[a] Note: valid in the range $a/t < 0.25$.

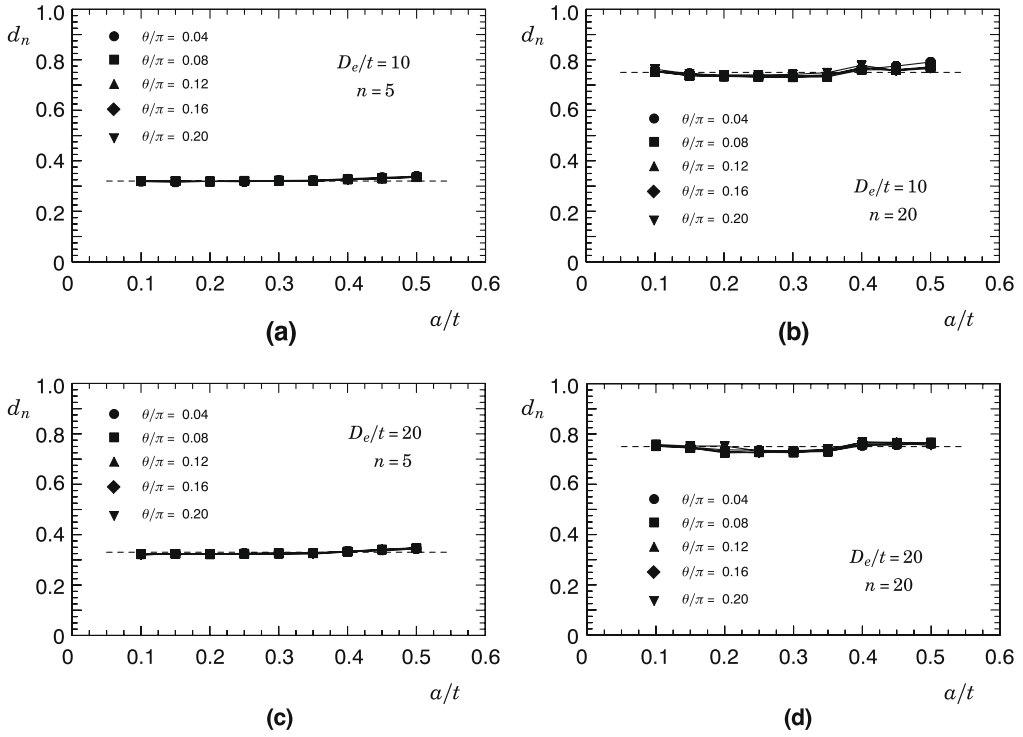


**Fig. 13.** Effect of strain hardening and crack configuration on the relationship between $J$ and CTOD as characterized by parameter $d_n$.

## 5. Effect of Ramberg–Osgood fit on the *J* estimation scheme

The fully plastic solution for the $J$-integral (CTOD) discussed thus far relies on an elastic–plastic power-hardening model based upon the $R$–$O$ form given by previous Eq. (1) to characterize the material's stress–strain behavior. In related work to estimate $J$ and CTOD in cracked structural components, Kim et al. [29–31] and Chattopadhyay [32], and earlier Zahoor [33], have raised some concern on the potential inability of the $R$–$O$ model to describe the stress–strain response in the full strain range which gives rise to rather inaccurate estimates of crack driving forces. Experimental trends in some specific materials, such as structural steels exhibiting Lüders bands, appear to support these observations as the power-law fit implied by the $R$–$O$ model does not necessarily provide a good description of the material's stress–strain relation, particularly at low strain levels corresponding to the yield plateau. However, these studies show no clear trends as their $J$ and CTOD predictions are rather strongly dependent on the stress–strain data set and on the strain range upon which the $R$–$O$ fit is conducted. It is

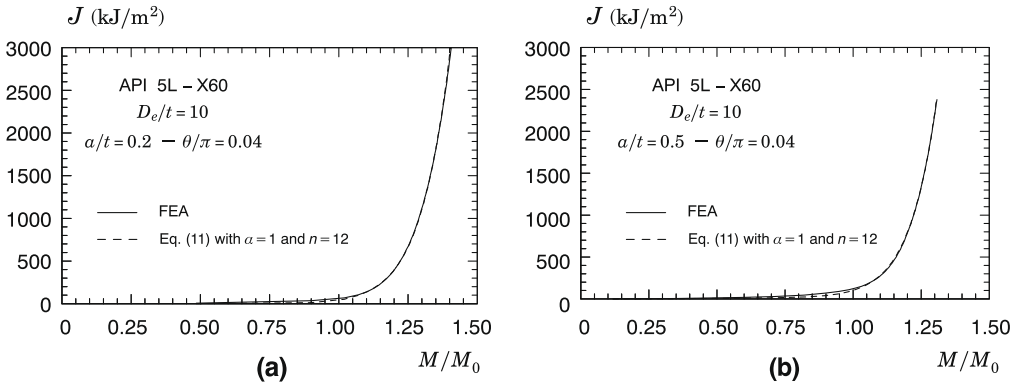


**Fig. 14.** $J$ vs. normalized bending moment for the pipe configuration with $D_e/t = 10$, $a/t = 0.2$ and 0.5, $\theta/\pi = 0.04$ and continuous hardening material.

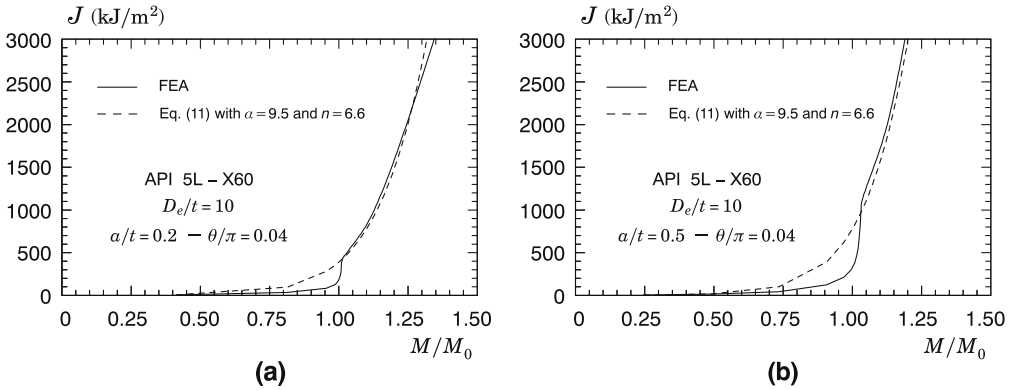


**Fig. 15.** $J$ vs. normalized bending moment for the pipe configuration with $D_e/t = 10$, $a/t = 0.2$ and 0.5, $\theta/\pi = 0.04$ and material having yield plateau.

beyond the scope of the present work to perform a detailed sensitivity analysis of the effect of $R$–$O$ fit on the proposed $J$ (CTOD) estimation scheme. This section examines the potential deviations in predictions of crack driving forces, as characterized by $J$, for key cracked configurations when a material's stress–strain response exhibiting a significant amount of Lüder strains is approximated by a $R$–$O$ power-law fit.

Figs. 14 and 15 show the evolution of the $J$-integral with normalized bending moment, $M/M_0$, for circumferentially cracked pipes with $D_e/t = 10$, $a/t = 0.2$ and 0.5, and $\theta/\pi = 0.04$. The material adopted in these analyses is a typical API 5L Grade X60 with rather different true stress vs. true strain response in the elastic to fully plastic transition region as displayed in Fig. 4b. In that plot, the solid line represents a pipeline steel with continuous strain hardening behavior [27] whereas the dashed line describes the stress–strain response for a pipeline steel displaying a Lüders plateau given in Ref. [28]. The $R$–$O$ parameters for both pipeline steels derived from fitting the corresponding true stress–true strain data using Eq. (1) are given in Section 3.2.

Consider first the results for the material with continuous strain hardening behavior displayed in Fig. 14a and b. Here, the predicted curves are derived from using Eq. (11) with $\alpha = 1$ and $n = 12$ in which factor $h_1$ is obtained by a parabolic interpolation of the $h_1$-values for $n = 5$, 10 and 20 given in previous Section 4. As could be expected, the predicted curves for both crack configurations ($a/t = 0.2$ and 0.5) are practically indistinguishable from the finite element results since the $R$–$O$ fit provides a very good description of the stress–strain data set. Now, direct attention to the variation of $J$ with $M/M_0$ for the material exhibiting a yield plateau shown in Fig. 15a and b. Similarly to the previous analyses, the predicted curves are derived from using Eq. (11) but with the $R$–$O$ parameters given by $\alpha = 9.5$ and $n = 6.6$; as before, factor $h_1$ is conveniently interpolated from the $h_1$-values for $n = 5$, 10 and 20. Over the loading range dominated by the effects of the Lüders strains ($0.75 \leq M/M_0 \leq 1.0$), the finite element results fall well below the predicted curves, particularly for the deep crack configuration. After this transitional behavior, however, both curves are essentially similar and provide no significant differences in the $J$ vs. $M/M_0$ relationship.

While rather limited, the results in Figs. 14 and 15 provide compelling evidence that the proposed estimation scheme can accurately characterize the crack-tip driving forces, $J$ and CTOD, in circumferentially cracked pipes subjected to bending load. This seems particularly true for larger loading and deformation levels ($M/M_0 \geq 1.1$—$1.21$), which would most likely be the case of interest in reeled pipes. Nevertheless, we consider the debate over the sensitivity of $J$ and CTOD estimates derived from the fully plastic solution on the $R$–$O$ power-law fit still valid. This issue should be addressed in future studies.

## 6. *J* estimation for circumferentially cracked pipes subjected to reeling

The accurate evaluation of the crack-tip driving forces during the reeling process and subsequent operation plays a key role in fitness-for-service analyses and integrity assessments of pipeline girth welds. To demonstrate the effectiveness of the methodology presented previously in describing adequately the crack-tip driving forces of in-service cracked configurations, this section examines the prediction of the maximum *J*-value attained during pipeline installation by the reeling method [1,2] based upon current defect assessment procedures for submarine pipelines such as DNV OS-F101 [34]. The verification studies conducted here compare predictions of the maximum *J*-values for circumferentially cracked pipelines with varying crack configuration based upon the fully plastic solutions described here with the corresponding crack-tip driving forces obtained directly from the finite element analyses presented in previous Section 3. Numerical simulation of the reeling is performed by considering a reel drum with diameter $\Phi_r$ = 15,000 mm modeled as the rigid surface represented in Fig. 3a. The analyzed pipes have outside diameter, $D_e$ = 344.5 mm (13.5 in.), thickness, $t$ = 20.6 mm ($D_e/t$ = 16.7) and external, circumferential surface flaws with length $2c$ = 100 mm ($\theta/\pi$ = 0.073) and different crack depth ($a$) over pipe wall thickness ($t$) ratios: $a/t$ = 0.1, 0.2, 0.3 and 0.4 (see Fig. 1). The material is an API 5L Grade X60 pipeline steel with 483 MPa yield stress ($\sigma_{ys}$) at room temperature (20 °C). Fig. 4b displays the true stress–strain data for this pipeline steel [26] which was utilized in the numerical computations.

Fig. 16a provides the evolution of crack-tip driving forces, as quantified by *J*, with increased load-line displacement (LLD) and varying $a/t$-ratios for the analyzed cracked pipes. The LLD is defined as previously illustrated in Fig. 3. The effect of crack depth, $a$, on *J* is amply demonstrated by the results in Fig. 16a. The crack-tip driving forces rise slowly in the initial stage of reeling (as characterized by LLD) and then more rapidly as the reeling continues. As could be expected, there is a strong effect of $a/t$-ratio on *J*, particularly as the crack depth increases. A maximum value of driving force (which can be interpreted as a "plateau" value) is reached at LLD = ~3000 mm for all $a/t$-ratios. This load level marks the pipe curvature at which the reeling process ceases to control the crack opening (see Fig. 3). Here, a large section of the pipe has entirely contacted the reel drum so that the strong bending loading which arises from the reeling process with increased LLD does not affect crack opening anymore.

The verification analysis to evaluate the maximum *J* values for the reeled cracked pipes based upon the fully plastic solutions described in Section 2.2 proceeds as follows. The applied bending moment entering into previous Eqs. (11) and (16) is determined from first evaluating the maximum bending strain which the reeled is subjected to and then computing the bending moment using available moment–strain relationships. Under pure bending, the longitudinal bending strain, $\varepsilon_z^b$, for a pipe with outside diameter, $D_e$, is given by

$$\varepsilon_z^b = \frac{D_e}{2R_b + D_e} \tag{25}$$

where $R_b$ is the bending radius. For the reeled pipe, the bending strain attains its maximum value, $\varepsilon_{z,max}^b$, when $R_b = \Phi_r/2$ yielding $\varepsilon_{z,max}^b = 0.0225$.

A simpler finite element analysis for the cracked pipes under pure bending (no contact with the rigid reel drum is employed) now characterizes the relationship between the applied bending moment and the longitudinal (bending) strains. Fig. 16b shows the moment–longitudinal strain response for all crack configurations considered. The figure also includes the evolution of $M$ with $\varepsilon_z^b$ for an uncracked pipe. The mechanical behavior characterized in terms of the moment–strain relationship for all analyzed configurations, including the uncracked pipe, is virtually unchanged with crack size and depends only on the mechanical properties of the material and on the $D_e/t$-ratio. Such features have important implications in defect assessment procedures as evaluation of the applied bending moment is more easily accomplished through a simpler finite element analysis for an uncracked pipe which generally demands less computational resources than the corresponding cracked pipe. The present findings are fully in accord with previous numerical results obtained by Østby et al. [35] for pipelines subjected to large plastic deformation under bending.

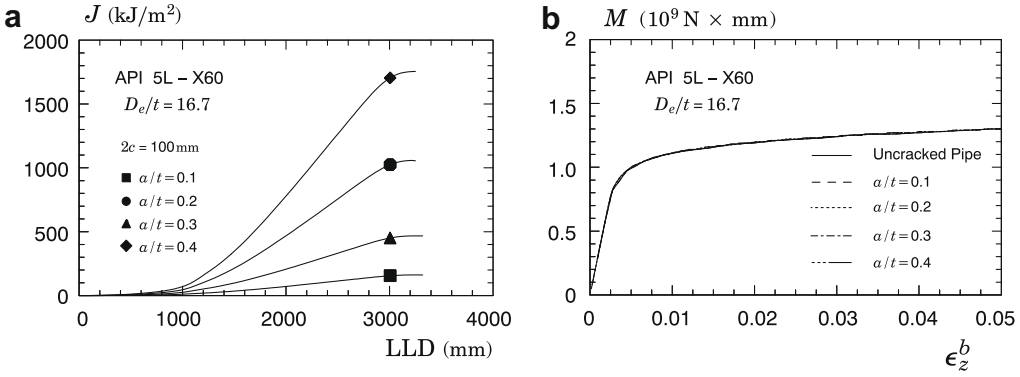


**Fig. 16.** (a) Crack-tip driving forces for the cracked reeled pipe with $2c$ = 100 mm and increased LLD for varying $a/t$-ratios and (b) Moment–longitudinal strain response for all analyzed crack configurations.

**Table 7**
Comparison of predicted (maximum) $J$-value based upon the fully plastic solutions and the numerical maximum $J$ attained in the reeling simulation for each analyzed cracked pipe.

| Pipe configuration ($a/t$) | $J_{reel}$ (kJ/m$^2$) | $J_{pred}$ (kJ/m$^2$) | $J_{reel}/J_{pred}$ |
|---|---|---|---|
| 0.1 | 161.0 | 167.1 | 0.96 |
| 0.2 | 467.0 | 463.7 | 1.01 |
| 0.3 | 1055.0 | 1022.9 | 1.03 |
| 0.4 | 1755.0 | 1682.2 | 1.04 |

Evaluation of the maximum $J$-value for the reeled cracked pipes follows from using Eqs. (11) and (16) with the bending moment, $M$, at the deformation level $\varepsilon^b_{z,max} = 0.0225$ determined from the moment–longitudinal strain response displayed in Fig. 13b. Further, factor $h_1$ corresponding to $D_e/t = 16.7$ and a material with $n = 12$ (the Ramberg–Osgood exponent derived from a curve fitting to the true stress–true strain data of Fig. 4b – see Section 3.2) is obtained based upon a parabolic interpolation using the $h_1$-values for $n = 5$, 10 and 20. Table 7 compares the predicted (maximum) $J$-value based upon the procedure outlined above, denoted $J_{pred}$, and the numerical maximum $J$ attained in the reeling simulation, $J_{reel}$, for each analyzed cracked pipe. Despite the inherent difficulties and the more complex stress state arising from the reeling analysis compared to a pure bending condition, errors in predicted maximum $J$-values are less than 4%. Such close agreement of fully-plastic estimates and finite element $J$-values provides strong support to use the present methodology in defect assessments of circumferentially cracked pipes under bending loading including reeled pipelines.

## 7. Summary and conclusions

This work provides an estimation procedure to determine the $J$-integral and CTOD for pipes with circumferential surface cracks subjected to bending load for a wide range of crack geometries and material properties based upon fully plastic solutions. In the present study, attention is directed to a circumferentially cracked pipe with surface flaws having different crack depth ($a$) over pipe wall thickness ($t$) ratios and varying crack length for different strain hardening properties and outside diameters ($D_e/t$). The methodology derives from fully plastic descriptions of $J$ and CTOD incorporating limit load solutions for the cracked component to determine nondimensional functions $h_1$ and $h_2$ applicable to a wide range of crack geometries and material properties characteristic of structural, pressure vessel and pipeline steels.

The extensive set of nonlinear, 3-D finite element analyses conducted in this study provides a definite full set of solutions for $J$ and CTOD which enters directly into fitness-for-service (FFS) analyses and defect assessment procedures of cracked pipes and cylinders subjected to bending load. The associated dimensionless $h$-values are derived from a least square fitting to the linear evolution of normalized $J_p$ with $(M/M_0)^{n+1}$ for quantities which follow a proportional dependence of $J_p$ on the applied loading ($M$). A strong linear relationship holds across all configurations with high ($n = 5$) and moderate ($n = 10$) strain hardening properties. For the low hardening material ($n = 20$), such strong linear relation is warranted for crack sizes in the range $a/t \leqslant 0.25$ which is well within the limits routinely adopted in design, fitness-for-service assessments as well as nondestructive testing examination.

Verification analyses conducted on reeled cracked pipes demonstrated the capability of the present fully plastic solutions in predicting the maximum $J$ values attained during the reeling process. Moreover, an exploratory sensitivity analysis to assess the robustness of the Ramberg–Osgood power-law fit to model the material's stress–strain response reveals a relatively minor effect of the power-law fit, particularly for larger loading and deformation levels beyond the Lüders strain range, in characterizing the crack-tip driving forces based upon the estimation procedure described here. While we have not explored other crack configurations and material properties, the relative operational simplicity compared to full 3-D analyses and the close agreement between predicted and finite element results provide a compelling support to adopt the present methodology as an engineering tool to estimate crack driving forces in routine fitness-for-service analyses.

It should be noted that a key feature in the success of the estimation procedure for $J$ and CTOD lies also in the accurate evaluation of the applied bending moment directly entering into Eqs. (11) and (12). Because the fully plastic solution for the crack driving forces depend upon $(M/M_0)^{n+1}$, small variations in load potentially lead to large changes in $J$ and CTOD, particularly for higher values of the strain hardening exponent. Employing a simple procedure to define the relationship between applied moment and global strain for the reeled cracked pipe did provide highly accurate maximum $J$-values, but the overall robustness of the approach for other crack configurations and loading conditions remain untested. An investigation along this line is in progress. Ongoing work with the fully plastic solution framework also focuses on deriving $h$-values for circumferentially cracked pipes under combined bending, tension and internal pressure as well as for overmatched girth welds and increased $D_e/t$-ratios.

## Acknowledgments

This investigation was supported by the Brazilian State Oil Company (Petrobras). The work of C. Ruggieri and M.S.G. Chiodo was also supported by the Brazilian Council for Scientific and Technological Development (CNPq). The authors are indebted to Eduardo Hippert Jr. and Guilherme V.P. Donato (CENPES-Petrobras) for his valuable contributions and useful

discussions. The authors also acknowledge Gustavo H.B. Donato and Luis F.S. Parise for assisting in the finite element modeling of the pipe specimens.

## References

[1] Manouchehri S, Howard B, Denniel S. A discussion of the effect of the reeled installation process on pipeline limit states. In: 18th International offshore and polar engineering conference (ISOPE), Vancouver, Canada; 2008.
[2] Wästberg S, Pisarski H, Nyhus B. Guidelines for engineering critical assessments for pipeline installation methods introducing cyclic plastic strain. In: 23rd International conference on offshore mechanics and arctic engineering (OMAE), Vancouver, Canada; 2004.
[3] Hutchinson JW. Fundamentals of the phenomenological theory of nonlinear fracture mechanics. J Appl Mech 1983;50:1042–51.
[4] Shih CF. Relationship between the *J*-integral and the crack opening displacement for stationary and extending cracks. J Mech Phys Solids 1981;29:305–26.
[5] Anderson TL. Fracture mechanics: fundamentals and applications. 3rd ed. Boca Raton: CRC Press; 2005.
[6] Saxena A. Nonlinear fracture mechanics for engineers. Boca Raton: CRC Press; 1998.
[7] Tada H, Paris PC, Irwin GR. The stress analysis of cracks handbook. 2nd ed. St. Louis: Paris Productions; 1985.
[8] British Standard Institution. Guide on methods for assessing the acceptability of flaws in metallic structures. BS7910; 2005.
[9] SINTAP: Structural Integrity Assessment Procedure for European Industry. Final procedure; 1999.
[10] American Petroleum Institute. Fitness-for-service, API RP-579-1/ASME FFS-1; 2007.
[11] Marie S, Chapuliot S, Kayser Y, Lacire MH, Drubay B, Barthelet B, et al. French RSE-M and RCC-MR code appendixes for flaw analysis: presentation of the fracture parameter calculation – Part I: general overview. Int J Pressure Vessels Pip 2007;84:590–600.
[12] Sumpter JDG, Turner CE. Method for laboratory determination of $J_c$, cracks and fracture, ASTM STP 601, American Society for Testing and Materials; 1976. p. 3–18.
[13] Cravero S, Ruggieri C. Estimation procedure of *J*-resistance curves for SE(T) fracture specimens using unloading compliance. Engng Fract Mech 2007;74:2735–57.
[14] Cravero S, Ruggieri C. Further developments in *J* evaluation procedure for growing cracks based on LLD and CMOD data. Int J Fract 2007;148:387–400.
[15] American Society for Testing and Materials. Standard test method for measurement of fracture toughness, ASTM E1820; 2001.
[16] Kumar V, German MD, Shih CF. An engineering approach to elastic–plastic fracture analysis. EPRI Report NP-1931. Electric Power Research Institute, Palo Alto, CA; 1981.
[17] Shih CF, Hutchinson JW. Fully plastic solutions and large scale yielding estimates for plane stress crack problems. Trans ASME J Engng Mater Technol – Ser H 1976;98:289–95.
[18] Dowling NE. Mechanical behavior of materials. 2nd ed. NJ: Prentice Hall; 1999.
[19] Zahoor A. Ductile fracture handbook. EPRI Report NP-6301-D, Electric Power Research Institute, Palo Alto, CA, vol. 2; 1989.
[20] Ainsworth RA. The assessments of defects in structures of strain hardening materials. Engng Fract Mech 1984;19:633–42.
[21] Kanninen MF, Popelar CH. Advanced fracture mechanics. New York: Oxford University Press; 1985.
[22] Ilyushin AA. The theory of small elastic–plastic deformations. Prikadnaia Matematica i Mekhanika (PMM) 1946;10:347–56 [in Russian].
[23] Gullerud A, Koppenhoefer K, Roy A, RoyChowdhury S, Walters M, Bichon B, et al. WARP3D: dynamic nonlinear fracture analysis of solids using a parallel computers and workstations. Structural research series (SRS) 607. UILU-ENG-95-2012, University of Illinois at Urbana-Champaign; 2004.
[24] Hughes TJ. Generalization of selective integration procedures to anisotropic and nonlinear media. Int J Numer Methods Engng 1980;15:1413–8.
[25] Moran B, Shih CF. A general treatment of crack tip contour integrals. Int J Fract 1987;35:295–310.
[26] Chiodo MSG, Ruggieri C. Failure assessments of corroded pipelines with axial defects using stress-based criteria: numerical studies and verification analyses. Int J Pressure Vessels Pip 2009;86:164–76.
[27] Silva MS. Fracture toughness and R-curve measurements for an API X60 pipeline steel using a direct current potential technique. M.Sc. Thesis. Faculty of Engineering (COPPE), Federal University of Rio de Janeiro; 2002 [in Portuguese].
[28] Petrobrás. ECA evaluation of marlim gas pipeline. Private Report; 2008.
[29] Kim YJ, Huh NS, Kim YJ. Enhanced reference-stress based *J* and crack opening displacement estimation method for leak-before-break analysis and comparison with GE/EPRI method. Fatigue Fract Engng Mater Struct 2001;24:243–54.
[30] Kim YJ, Huh NS, Kim YJ. Effect of lüders strain on engineering crack opening displacement estimations for leak-before-break analysis: finite element study. Fatigue Fract Engng Mater Struct 2001;24:617–23.
[31] Kim YJ, Huh NS, Kim YJ, Choi YH, Yang JS. On relevant Ramberg–Osgood fit to engineering non-linear fracture mechanics analysis. J Pressure Vessel Technol (ASME Trans) 2004;126:277–83.
[32] Chattopadhyay J. Improved *J* and COD estimation by GE/EPRI method in elastic to fully plastic transition zone. Engng Fract Mech 2009;73:1959–79.
[33] Zahoor A. Evaluation of *J*-integral estimation schemes for flawed through wall pipes. Nucl Engng Des 1987;100:1–9.
[34] Det Norsk Veritas. Submarine pipeline systems. DNV–OS–F101; 2007.
[35] Østby E, Jayadevan KR, Thaulow C. Fracture response of pipelines subjected to large plastic deformation under bending. Int J Pressure Vessels Pip 2005;85:201–15.
[36] API Specification for 5L Line Pipe – American Petroleum Institute API, 42nd ed.; 2000.
[37] American Society for Testing and Materials. Standard test methods and definitions for mechanical testing of steel products. ASTM A370; 2009.
[38] Silva LAL, Cravero S, Ruggieri C. Correlation of fracture behavior in high pressure pipelines with axial flaws using constraint designed test specimens – Part II: 3-D effects on constraint. Engng Fract Mech 2006;73:2123–38.